arXiv:2610.20834v1 [cond-mat.mtrl-sci] 14 Oct 2026

# Identifying intercalation electrodes for electrochemical ion recovery and desalination

Sougat Purohit[1], Andreas Kuhlmann[2,3], Marten Huck[2,3], Hans-Georg Steinrück[2,3], and Gopalakrishnan Sai Gautam[1,*]

[1]Department of Materials Engineering, Indian Institute of Science, Bengaluru, 560012, India

[2]Institute for a sustainable Hydrogen Economy (IHE-1), Forschungszentrum Jülich GmbH, An der Deutschen Welle 7a, Jülich 52428, Germany

[3]Institute of Physical Chemistry, Rheinisch-Westfälische Technische Hochschule Aachen, Landoltweg 2, Aachen 52074, Germany

[*]Email: saigautamg@iisc.ac.in

**Abstract**

Water sources serve as a requirement for human consumption, industrial, and agricultural needs and a resource for valuable ions. Appropriate treatment of water that captures ions from the aqueous solution can give rise to suitable 'products', such as critical ions (such as $Li^+$) in selective ion recovery and usable water in the case of desalination (i.e., removal of non-essential ions). Among myriad ion capture techniques, we focus on electrochemical methods using intercalation electrodes, an energy-efficient approach capable of both selectively extracting specific ions or non-selectively extracting multiple ions from diverse water sources. However, practical realization of electrochemical ion capture requires the use of robust cation intercalation electrodes, with the state-of-the-art olivine-$FePO_4$ and spinel-$Mn_2O_4$ exhibiting several shortcomings. Thus, we develop a high-throughput computational workflow to identify potential intercalation electrodes for both ion recovery and desalination from a pool of 20,414 Li, Mg, Ca, Na, and/or K-containing structures from the Materials Project database. Based on the construction of Pourbaix diagrams relevant for electrodes operating under seawater conditions, modifying criteria used for defining metastability in seawater, computing average intercalation voltages and the extent of metastability of electrode structures, and computational graphs to encode ionic selectivity, we identify a total of 11 promising electrodes for selective ion recovery and one possible desalination electrode. The promising materials identified in this work include $Fe_2(MoO_4)_3$, $Li_3Fe_2(PO_4)_3$, $LiFeP_2O_7$ for selective Li-recovery. Our study provides thermodynamic insights, qualitative trends, and a promising list of intercalation electrodes for experimental testing that should advance the field of electrochemical ion recovery.

## 1 Introduction

Conserving potable water and managing industrial effluents are crucial in an era of increasing salinity of freshwater resources caused by rising sea levels and anthropogenic activities [1]. Desalination, the process

of separating ions from water, can turn the challenge of increasing salinity into economic opportunities by sustainably extracting desired ions normally found in saline water (e.g., Li, Mg, K, etc.) and/or by producing clean water [2, 3]. Note that the objective of desalination is generally to produce cleaner water suitable for drinking, irrigation, or disposal post industrial usage. On the other hand, selective ion recovery [4,5] involves directly extracting a specific ion from salt water and/or waste water sources. Importantly, both desalination and selective ion recovery rely on similar thermodynamics as their working principles, with differences in the eventual 'product'.

With respect to ion recovery, one critical element that can be sustainably extracted from water-based sources is Li, the electroactive component of the most widely used energy storage technology, namely the Li-ion battery (LIB). The global push for renewable energy (and its associated storage) is expected to disrupt Li supply in the near future due to continuously increasing demand and uneven distribution of Li worldwide [6–8]. For instance, the Li-rich brines of South America constitute 42% of the global Li reserves [9] and rely on slow and water-intensive solar thermal evaporation followed by chemical separation of Li from the leftover salt for Li extraction [10]. In this context, direct Li extraction (DLE [11–13]) from aqueous sources provides a sustainable method to extract Li from non-conventional sources like geothermal brines [14], seawater [15–17], wastewater from battery recycling [18, 19], as well as from effluents of oil and gas plants [20]. While DLE from these sources involves selectively capturing $Li^+$ in the presence of competing cations, such as $Na^+$, $K^+$, $Mg^{2+}$, and $Ca^{2+}$ [13, 17, 21–23], desalination requires capturing all (possible) ions, including $Li^+$. Note that the extent to which "all" ions must be removed for desalination also depends on the overall composition of the water source, the specific use case (drinking, industrial or agricultural) and the respective regulatory specifications [24, 25].

Traditionally, desalination involves energy-intensive thermal evaporation of water, leaving behind salts [26,27], with the recovery of clean water via condensation. However, the most widely used industrial technique for seawater desalination is reverse osmosis (RO) [28–32], where pressure gradients force water through a selectively permeable membrane that separates water from dissolved ions. One limitation of RO processes is the expensive semi-permeable membrane, which can be susceptible to damage and fouling upon repeated use [33,34]. Moreover, RO by construction is not selective to a given element, such as Li, making it unsuitable for direct mineral extraction from aqueous sources. Thus, it is important to develop common technological platforms (or frameworks) that can be leveraged for either ion recovery or desalination, depending on the water source and the desired product.

Other techniques of ion removal from aqueous sources include hydrometallurgical methods involving the addition of precipitating solvents [35–37], chromatography [38–40], and electrochemical methods [5,11,41–46]. Out of these techniques, we focus on electrochemical methods since they have the potential to act as common technological framework for both ion recovery and desalination, are typically less energy-intensive, and exhibit the versatility to handle various solutions (e.g., different concentrations of salts in solution). Notably, the choice of electrodes and their selectivity to various ions, applied potentials, and other operating conditions (temperatures, flow rates of solutions, etc.) can be tuned such that a given electrochemical setup can be used for either ion recovery (for mineral extraction) or desalination (for clean water generation), as schematically displayed in **Figure S1** of the supporting information (SI). Through the rest of the manuscript, we will employ the terminology, 'ion capture' to refer to either desalination or ion recovery.

Among the multiple variants of electrochemical techniques, we focus on employing intercalation electrodes that can extract ion(s) from a solution, a process with operating principles similar to LIBs [8, 47–49]. Intercalation electrodes work by absorbing ions (from the solution) into the available lattice (interstitial)

sites in their structure under an applied potential/current, with cations usually intercalating better compared to the larger-sized and oppositely-charged anions (such as $Cl^-$). Here, we screen for materials that can be suitable for capturing cation(s), i.e., those that can act as negative electrodes in an electrochemical setup (**Figure S1**), while we assume anions in the solution to be simultaneously captured by a capacitive or a conversion-type positive electrode [5, 8, 47]. The efficient capture of cation(s) depends on the properties of the intercalation electrodes, which makes ion capture performance a material-dependent property. Hence, to improve ion capture, promising intercalation electrodes and an improved understanding of the associated mechanisms and processes are required.

So far, intercalation electrodes that have been employed for ion capture from aqueous solutions include olivine-$FePO_4$ [11, 16, 50] and $Mn_2O_4$ (or $MnO_2$ equivalently) polymorphs, such as the spinel [18, 51–53]. $FePO_4$ and $Mn_2O_4$ have been explored due to their ability to intercalate a variety of ions simultaneously and reversibly (for desalination) and/or their relatively high selectivity for $Li^+$ over other cations (for ion recovery). However, both $FePO_4$ and $Mn_2O_4$ electrodes are limited by different factors, such as the poor electronic conductivity of olivine-$FePO_4$ resulting in slow intercalation kinetics [54] and the poor structural stability of spinel-$Mn_2O_4$ due to Mn dissolution during cycling [55, 56]. Attempts to mitigate the such shortcomings include carbon coating the $FePO_4$ to improve the intercalation kinetics [26] and doping Ni in $Mn_2O_4$ to improve its structural stability [57]. Also, there have been attempts to make $LiFePO_4$ more selective towards $Li^+$ by using a $TiO_2$ coating [16]. Overall, the literature has focused on employing morphological/structural/compositional modifications of olivine-$FePO_4$ and spinel-$Mn_2O_4$ for ion capture. As a complementary pathway to improve electrochemical ion capture, we propose a high-throughput computation-driven approach to explore different chemical and structural spaces, and identify novel and sustainable electrodes with intrinsically better properties.

The cation intercalation electrodes in ion capture processes absorb/release $Li^+$ (or by extension, other cations), via the (de)intercalation mechanism with the application/removal of an external potential/current, which is identical to the operation of a positive electrode (cathode) in LIBs. Thus, the extensive research on LIB and beyond-LIB cathodes provides immense data to identify novel electrodes that can achieve better ion capture efficiencies than either olivine-$FePO_4$ or spinel-$Mn_2O_4$ based electrodes. Thus, in this work, we use the Materials Project (MP) database [58], built from high-throughput density functional theory (DFT [59, 60]) calculations as the primary data source, and apply material-specific screening criteria (as described below) to find promising electrode candidates for ion capture.

For a material to be useful as an ion capture electrode, there are constraints the material must satisfy, which are different from the constraints typically used for battery cathode selection [61–63]. For instance, LIBs and analogous battery technologies contain non-aqueous electrolytes with wider voltage stability windows (∼3-4 V [64–67]) than water (∼1.23 V [68]) that allow for higher operating voltages. Thus, water being the medium for ion capture limits the range of applied potentials, versus standard hydrogen electrode (SHE), within which an electrode has to operate. Moreover, the potential dissolution of non-electroactive species (such as $Mn^{2+}$ [69,70]) can detrimentally affect the long-term stability and cycle life of the electrode, making stability of the material in aqueous solutions an important criterion. However, information on the aqueous stability of materials is not readily available in any computational/experimental database. Additionally, we require materials with good ionic selectivity, i.e., intercalate only the desired ion among other ions present in the solution, for ion recovery, while we require electrodes with low selectivity for desalination. Thus, aqueous stability, 'optimum' intercalation voltages, and ionic (non-)selectivity are important screening criteria for identifying novel electrodes for electrochemical ion capture.

To determine the aqueous stability of potential electrode materials, we make use of DFT-based Pourbaix diagrams [71], which are phase diagrams built with semi-grand canonical boundary conditions and plotted on an electrode potential (referred to as applied potential in this work) vs. pH scale at a given temperature (usually 298 K) [72]. Pourbaix diagrams have been previously employed in the high-throughput screening of photocatalysts for $CO_2$ reduction [73], and in the identification of water-stable metals, intermetallics, and metal oxides [74]. Moreover, recent works by Du et al. [75] and Ruiz et al. [76] extend the utility of Pourbaix diagrams for exploring interfacial properties and phase prevalence of materials. Similarly, ion capture presents an additional challenge of the electrode having to be stable in an aqueous solution containing additional non-electroactive elements (as compared to pure water), which can affect the aqueous stability of the electrode. Thus, we introduce a modified metastability formalism within our calculated Pourbaix diagrams that incorporates the presence of common ionic species in seawater-based brine sources, such as Cl, S, Na, and Mg, to evaluate the stability of potential electrodes in multi-component aqueous solutions. Note that the most critical cation to be captured in a desalination process is usually $Na^+$, given its large abundance in seawater.

In this work, we utilize DFT-calculated Pourbaix diagrams, develop associated screening criteria, and construct computational graphs to identify promising intercalation electrodes for electrochemical ion capture. We introduce important modifications on the Pourbaix diagram construction to include (*i*) additional ions in the aqueous phase that affect the stability of electrodes; (*ii*) a re-defined electrode metastability criterion in seawater that is extendable to any desired aqueous composition; and (*iii*) intercalation voltages under operating conditions to identify promising electrodes. Overall, we screen 20,414 structures from MP and identify 11 promising electrodes for ion recovery (with high selectivity) and one desalination electrode (with low selectivity) that can operate in seawater. We provide detailed descriptions and schematics of all the candidates identified in this work, with a special emphasis on the candidates that share similarities with experimentally known structures.

Notably, we identify pyrophosphate-$LiFeP_2O_7$, anti-NASICON-$Fe_2(PO_4)_3$, and garnet-like-$Fe(MoO_4)_2$ as the most promising Li-selective electrodes for Li-ion recovery. Additionally, we find 8 structures, including orthophosphates, alluaudites, spinels, perovskites, and hollandite-like structures that are selective towards one of the seawater-abundant cations, namely, Na, K, Mg, and Ca. Besides electrodes for ion recovery, we find 8 electrodes, that can intercalate two, three, or four of Li, Na, K, Mg, and Ca. For instance, we find novel (theoretical) electrodes that can simultaneously intercalate $Ca^{2+}$ and $Mg^{2+}$, namely, monoclinic-$FePO_4$ and triclinic-$Fe_2(MoO_4)_3$, with possible utility in water-softening. While we do not find any electrode that intercalates all five cations, olivine-$FePO_4$ is the most promising desalination electrode that we identify given that it can intercalate four (Li, Na, K, and Mg) out of five cations considered. Finally, our work provides a robust, systematic, computation-driven screening strategy and identifies intercalation electrodes for electrochemical ion capture, which should improve the associated process efficiencies in the near term and enable a successful transition to a sustainable water utilization and energy future.

# 2 Methods

## 2.1 Workflow

**Figure 1** provides a schematic of the workflow used in this work, involving four distinct steps. We start by querying first principles calculated data from MP for materials that can potentially intercalate Li, Na,

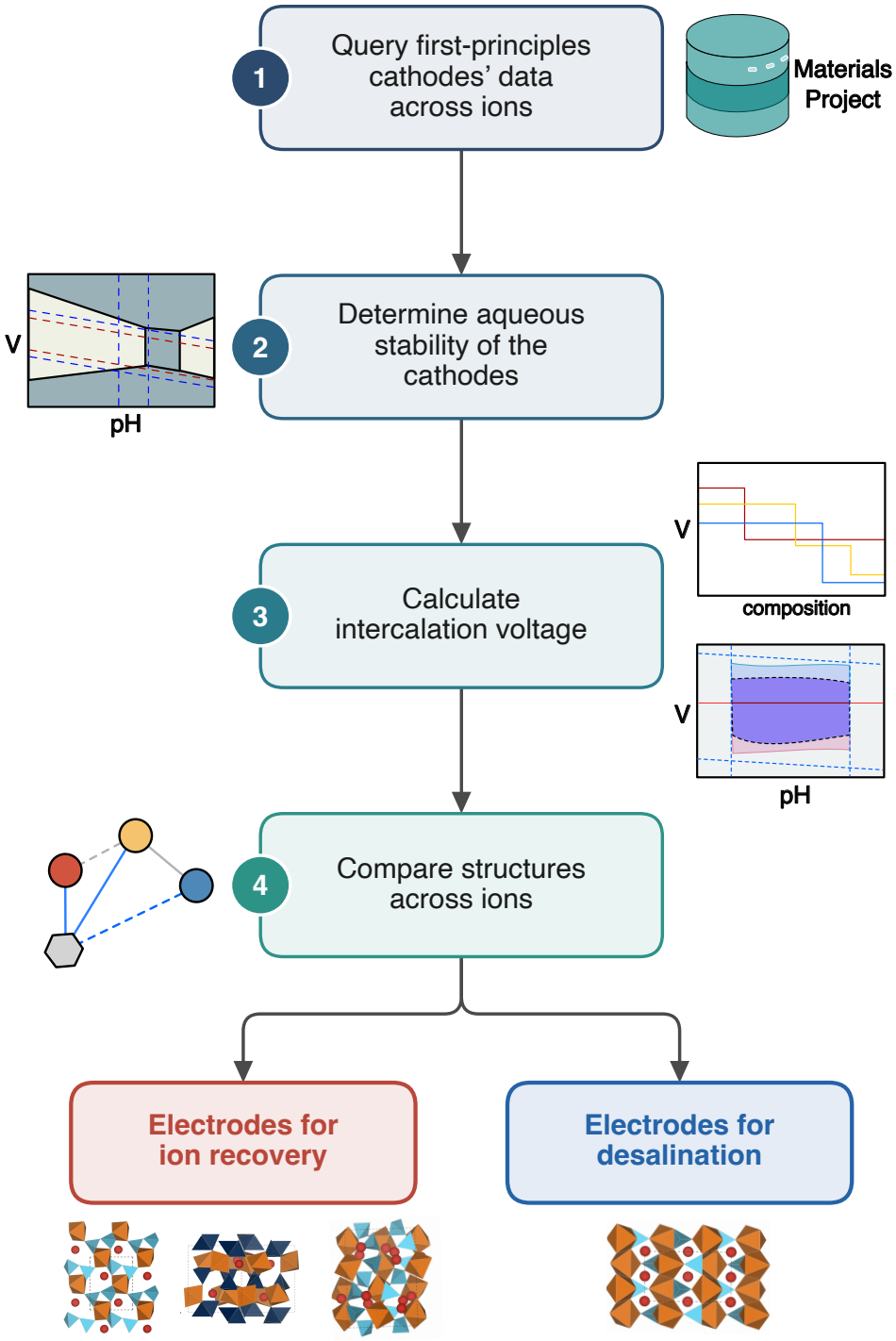



Figure 1: Schematic of the workflow used in the current work, including obtaining DFT data, generating seawater Pourbaix diagrams and evaluating thermodynamic (meta)stability, calculating operating voltages, and identifying unique structural candidates that are suitable for electrochemical ion recovery and desalination.

K, Mg, and Ca (see **Section 2.2**). In the second step, we generate Pourbaix diagrams for all the queried electrode compositions by including the four most abundant elements present in seawater (besides H and

O), namely, Cl, Na, S, and Mg, to quantify the aqueous (seawater) stability of the electrodes. We refer to the generated Pourbaix diagrams as the 'seawater Pourbaix diagrams' (**Section 2.3**). In the third step, for all electrode candidates that are (meta)stable in seawater (**Section 2.4**), we evaluate the thermodynamic average intercalation voltages and the extent to which the metastable phases can exist across the pH and potentials in seawater (**Section 2.5**). Finally, we compare the electrode-frameworks (**Section 2.6**) across the five different electroactive cations (i.e., Li, Na, K, Mg, and Ca), to identify frameworks that are selective to a single ion (for ion recovery) and structures that can intercalate multiple ions (for desalination). We make this step-wise workflow available as a `python` package named 'seawater Pourbaix intercalation cation electrode screening' (`SPICES`) on the GitHub repository associated with this work.

## 2.2 Data and querying process

We summarize the querying of structural and thermodynamic data for Li, Na, K, Mg, and Ca based materials from MP (v2025.06.09), in panels a and b of **Figure 2**. Since intercalation electrodes contain at least one redox-active transition metal (TM) and one anion to maintain charge neutrality with (de)intercalation, we searched for solids containing at least one and at most three TMs and at least one and at most three anions. We chose at most three TMs and anions to keep the number of possible elemental combinations computationally tractable. Also, we required that the solids contain at least one of the electroactive ions among Li, Na, K, Mg, and Ca, reflecting the given structure's ability to host one of the cations considered. Note that we excluded recent mixing corrections on total energies [77] that have been made available for a small fraction of materials in the MP to maintain energy (and voltage) consistency across the diverse chemical space screened here.

For the choice of TMs, we included all $3d$ metals that show redox activity (i.e., from Ti to Cu), and selected $4d$ and $5d$ metals that have shown redox activity and have been part of battery cathode explorations, as highlighted in blue in **Figure 2a** [78–84]. All anions considered are shown in yellow in **Figure 2a**. Our search lead us to 12,536 Li, 3,598 Mg, 1,344 Ca, 1,783 Na, and 1,153 K containing structures, resulting in a total of 20,414 possible electrode materials, as shown by the cyan bars in **Figure 2b**. The disproportionately high number of Li-containing structures in **Figure 2b** is a consequence of the heavily investigated LIB cathode chemical space and is not necessarily an indication that there are intrinsically more Li intercalating structures.

## 2.3 Constructing seawater Pourbaix diagrams

While Pourbaix diagrams involving elemental systems are well documented [71], our queried electrodes contain multiple elements, requiring the construction of challenging multi-element Pourbaix diagrams [85]. Hence, we use the thermodynamic framework [86–89] encoded in the "`pourbaix_diagram`" module of the `pymatgen` [90] package to generate the required multi-element Pourbaix diagrams. The `pourbaix_diagram` module combines experimental ionic solubility data [91, 92] and computational solid phase data, as documented in MP, and identifies phases that minimize the semi-grand canonical potential that is open to H and O (also referred to as the 'Pourbaix potential'). In all, we constructed 7,806 Pourbaix diagrams spanning over 1,046 distinct multi-element systems, based on our queried MP data. Mathematical details of the Pourbaix potential and the associated thermodynamic formalism can be found in **Section S2**.

Example Pourbaix diagrams involving olivine-$LiFePO_4$ are shown in panels c and d of **Figure 2**, indicating the regions of pH and applied potentials (in V vs. SHE) where the phase of interest is thermodynamically

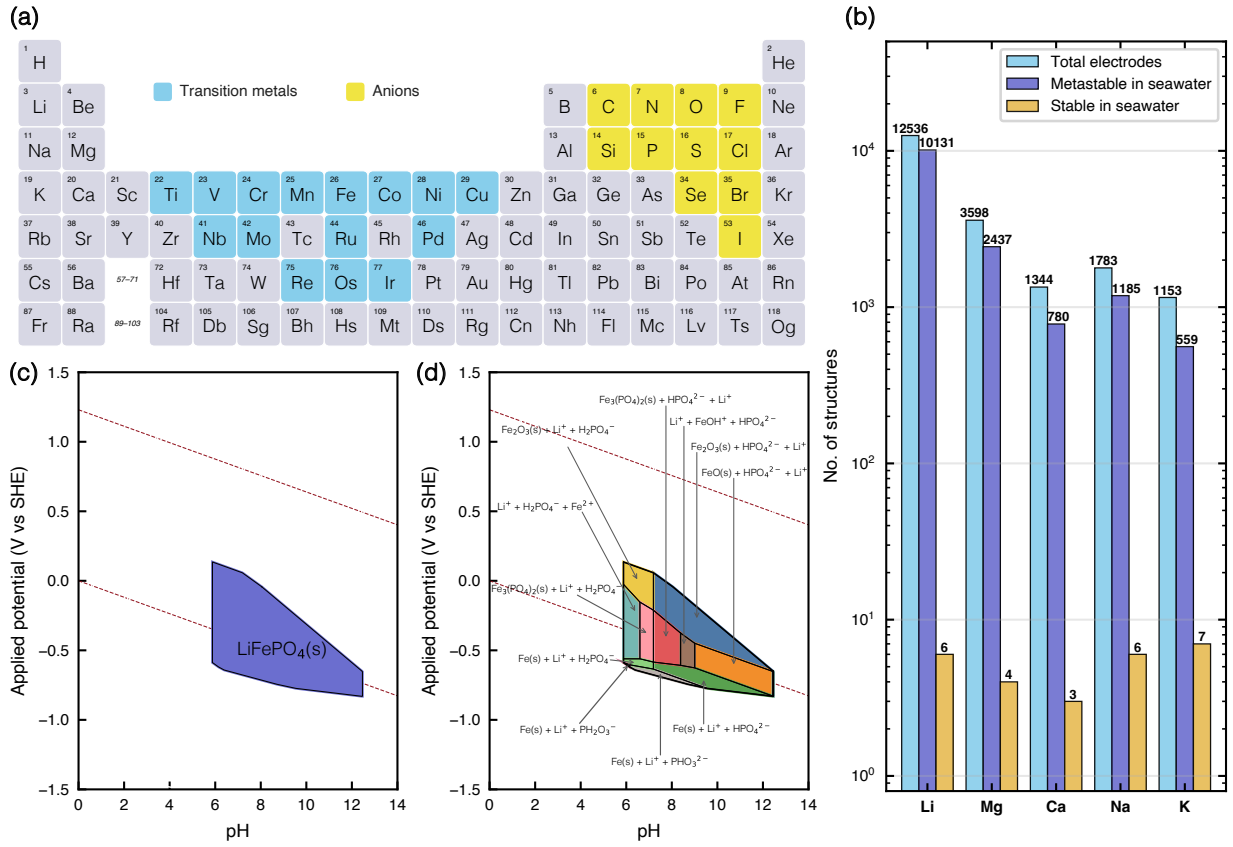



Figure 2: (a) Periodic table snippet showing redox-active TMs (blue) and anionic (yellow) elements considered in our search for possible ion capture electrodes. (b) Bars representing the total number of queried (cyan), seawater metastable (blue), and seawater stable (yellow) electrode structures containing different electroactive ions. (c), (d) Pourbaix diagrams showing the thermodynamic stability of $LiFePO_4$ at aqueous concentrations of (c) [Li] = 0.75 M, [Fe] = 0.25 M and [P] = 0.33 M and (d) in the dilute limit of [Li] = [Fe] = [P] = $10^{-6}$ M. The arrow marks in panel d refer to the decomposition products that form in preference to $LiFePO_4$ co-existing with the aqueous solution at different pH and applied potentials.

stable (for example, the purple region in **Figure 2c**). Note that water is stable only over a limited window in any Pourbaix diagram, as indicated by the region within the dashed red lines in **Figure 2c** and **d**, with the red lines corresponding to hydrogen and oxygen evolution reactions. Thus, an intersection of a solid's region of stability and the water stability window indicates that the solid is thermodynamically stable in water, over the intersected region.

The $LiFePO_4$ Pourbaix diagrams also illustrate the effect of the composition of the aqueous medium on the solid's aqueous stability. For example, in an aqueous solution containing large concentrations of ions, namely, [Li] = 0.75 M, [Fe] = 0.25 M, and [P] = 0.33 M, we observe $LiFePO_4$ to be thermodynamically stable (purple region in **Figure 2c**) across a range of pH and applied potentials. However, in a dilute solution containing [Li] = [Fe] = [P] = $10^{-6}$ M, $LiFePO_4$ does not appear as a stable phase on the Pourbaix diagram at any pH or applied potential, indicating its instability. Indeed, across a subset of the pH and applied potential region where $LiFePO_4$ is stable in **Figure 2c**, we observe different Fe and Li-containing phases to coexist in preference to $LiFePO_4$ (each distinct colour in **Figure 2d**, corresponds to different combination of stable phases). Thus, our observation with $LiFePO_4$ clearly shows, perhaps not surprisingly, that the

stability of a solid is influenced by its surrounding aqueous (solution) composition.

We fixed the concentration of ions in the aqueous medium to be the same as the average seawater concentration in our Pourbaix diagram constructions, given that many brines are derived from seawater. Note that while seawater contains numerous elements, the six most abundant species are $Cl^{-}$, $Na^{+}$ , $Mg^{+2}$, $SO_4^{-2}$, $Ca^{+2}$, and $K^{+}$, as shown in **Figure S2a** of the SI, while all other elements/species occur in low concentrations (<0.01 M). Since the computational complexity of a Pourbaix diagram increases significantly with every additional element (see **Figure S2b**) [87], we only added the top four abundant seawater elements, i.e., Cl, Na, Mg and S, to the solution phase in addition to the elements present in the solid. The resultant Pourbaix diagrams that are generated are our seawater Pourbaix diagrams, which we subsequently use to estimate the (meta)stability of the queried solid phases. More details on the construction of the seawater Pourbaix diagrams, including modifications made to the Pourbaix potential, are documented in **Section S3** of the SI. While we consider the average seawater concentration in our work, our framework can be trivially updated to consider any other desired aqueous composition.

## 2.4 Determining aqueous (meta)stability

Since seawater exhibits an average pH of 8 [93], we don't expect seawater to be stable under highly basic (e.g., pH =12) or highly acidic (e.g., pH = 2) conditions, and hence set aside a pH range of 7−8.5 as the region of stability of seawater. Note that we use seawater as a proxy in our work, but our method can be employed for any solvent conditions encountered in geothermal brines. Additionally, we shift the hydrogen evolution line by −0.3 V vs. SHE and the oxygen evolution line by +0.5 V vs. SHE to account for overpotentials for the hydrogen and oxygen evolution reactions [68], resulting in the expansion of the water stability window from 1.23 V to ∼2 V. Thus, we refer the 'seawater stability window' as the combination of the applied potential range of ∼2 V and a pH range of 7−8.5, as highlighted by the hashed blue area in **Figure 3a**. To determine the seawater stability of each of the queried structures, we examined the overlap between the seawater stability window, and the stability region of the electrode, where an overlap indicates that the electrode can be stable in seawater.

Upon computing the seawater stability for all the queried electrodes, we find only 6 Li, 4 Mg, 3 Ca, 6 Na, and 7 K structures to be stable in seawater, as indicated by the yellow bars in **Figure 2b**. The list of seawater stable electrodes, which have a stable domain within the seawater-stability window are compiled in **Table S2** of the SI. Surprisingly, the widely used Li-recovery electrodes that have been demonstrated to work with seawater-like brines, olivine-$LiFePO_4$ and spinel-$LiMn_2O_4$ [11, 16, 18, 50–52], are not among the list of stable electrodes in **Figure 2b**. This suggests that both $LiFePO_4$ and $LiMn_2O_4$ could be metastable in seawater and highlights the need to evaluate and quantify the extent of 'reasonable' metastability that allows electrodes to function in seawater.

Previous work has shown that solid phases can be assumed to be metastable in water if at least one of the stable decomposition products in the aqueous medium is a solid, and the energy of decomposition is ≤0.5 eV $atom^{-1}$ [89]. The basis for this metastability criterion is that solid-solid transitions typically exhibit high activation barriers, indicating that decomposition processes with 'small' thermodynamic driving forces (≤0.5 eV $atom^{-1}$) may not be kinetically active. Additionally, a solid decomposition product, if formed, can create a protective coating over the original decomposing solid to prevent further decomposition. While this metastability criterion was developed for phases in dilute aqueous solutions, we modified and extended this criterion to our seawater Pourbaix diagrams (see **Sections S5** and **S6** for details).

To modify the metastability criterion, we estimated the decomposition energy of olivine-$LiFePO_4$ in

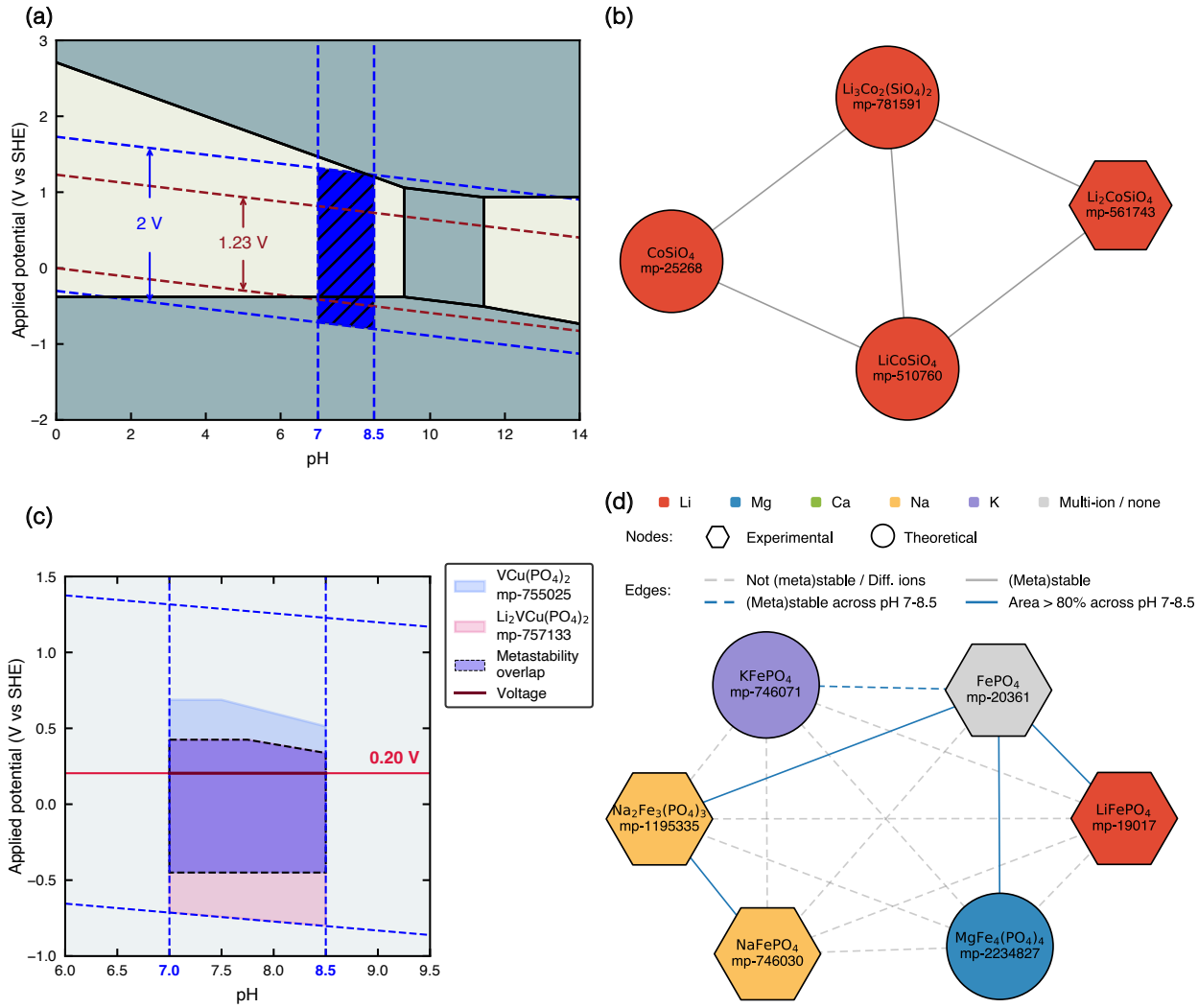



Figure 3: (a) Sample Pourbaix diagram showing the seawater stability window in hashed blue. (b) Sample computational graph generated for the $CoSiO_4$ host. The text annotations provide the MP ID for each intercalated structure constituting the graph. (c) Zoomed in seawater stability window (area within the dashed blue lines) showing the intersection of the metastability areas of an intercalated-deintercalated ($Li_2VCu(PO_4)_2$-$VCu(PO_4)_2$) pair of structures and their associated operating voltage of Li (de)intercalation (solid red line). (d) A sample computational graph of olivine-$FePO_4$ host, which unlike panel (b), encodes information across all the five electroactive ions considered. Since olivine-$FePO_4$ can intercalate four different cations, the graph contains nodes of four colors, namely, red (containing or exchanging $Li^+$), blue ($Mg^{+2}$), yellow($Na^+$) and purple($K^+$). The gray colored $FePO_4$ node represents a fully deintercalated structure that can intercalate multiple ions. The graph also encompasses information about the metastability/co-existence of pairs of structures via distinct edges.

seawater, which is $\leq$0.28 eV atom$^{-1}$ across the seawater stability window, with an Fe-containing solid decomposition product (see **Figure S4a**). Since olivine-$LiFePO_4$ has shown the ability to recover Li from brines [11,16,50] and we would want any new electrode material to be at least as (meta)stable as $LiFePO_4$, we selected a decomposition energy threshold of 0.3 eV atom$^{-1}$ instead of the previously used 0.5 eV atom$^{-1}$ threshold [89]. Additionally, it is desirable for the solid decomposition product that forms to be in the deintercalated state (i.e., without containing Li in the case of $LiFePO_4$) so that it does not trap any of the

working ions from the intercalation electrode. Also, it is undesirable for the decomposed solid to be an element (e.g., $LiFePO_4$ decomposing to form Fe), since pure elements, especially metals, are unlikely to form protective layers that are permeable to the working ion. Thus, our modified metastability criterion for any identified electrode is that the structure should form a non-elemental solid decomposition product with a maximum decomposition energy of 0.3 eV $atom^{-1}$ within the seawater stability window (see **Section S6**).

Note that Pourbaix diagrams are constructed using non-H and non-O elemental ratios that are chosen to match the elemental ratios of the solid under consideration [76]. For example, to evaluate the aqueous stability of solid $LiFePO_4$, the elemental ratios of the corresponding Pourbaix diagram has to be Li:Fe:P = 1:1:1. Thus, as long as the elemental ratios of the Pourbaix diagram matches the solid of interest, the decomposition energy at any pH and potential is simply the difference between the solid's Pourbaix potential and the sum of the Pourbaix potentials of the corresponding decomposition products. However, in our seawater Pourbaix diagrams, the elemental ratios of the decomposing solid do not always match those of the Pourbaix diagram due to the presence of additional elements in seawater (e.g., Cl) in non-dilute limits. Thus, to evaluate the decomposition energy of a queried electrode in a seawater Pourbaix diagram (see **Section S5**), we *i*) identify possible species that can react with the solid to form the decomposition products at each pH and potential, *ii*) enumerate all possible reactions, and *iii*) identify the reaction that yields the highest decomposition energy (i.e., maximizing the thermodynamic driving force). We subsequently compare the highest decomposition energy with the 0.3 eV $atom^{-1}$ threshold.

Using our modified metastability criterion, we found 10,131 Li, 2,437 Mg, 1,344 Ca, 1,185 Na, and 559 K phases to be metastable in seawater, as indicated by the violet bars in **Figure 2b**. As expected and per our definition, our modified criterion identifies both olivine-$LiFePO_4$ and spinel-$LiMn_2O_4$ as metastable in seawater, in agreement with experimental observations so far. Once we identify a structure to be metastable, we can project the region within the seawater stability window of the corresponding Pourbaix diagram where the structure is metastable. As an example, we have shown the metastability regions of $VCu(PO_4)_2$ (blue region) and $Li_2VCu(PO_4)_2$ (pink region) in the magnified version of the seawater Pourbaix diagram in **Figure 3c**.

## 2.5 Estimating (de)intercalation voltages and metastability overlap

The materials that have been shortlisted as metastable could − in principle − be metastable across any region within the seawater stability window. Thus it is important to examine whether the regions of metastability overlap for an electroactive ion intercalated structure as well as its corresponding deintercalated host, similar to the overlap seen (dark purple region) in the case of $Li_2VCu(PO_4)_2$-$VCu(PO_4)_2$ in **Figure 3c**. Equally important is to ascertain whether the queried phases are metastable at their corresponding ion intercalation voltage, i.e., do the structures remain metastable as they exchange electroactive ion(s). To address these aspects, we computed the average topotactic intercalation voltages of all the shortlisted frameworks using the Nernst equation and based on DFT-calculated total energies from MP [94].

To determine topotactic average voltages, we need to identify intercalated-deintercalated structure 'pairs' that are 'similar' to one another, since topotactic (de)intercalation occurs with minimal changes in the 'host' (host is the structure without the electroactive ion). While some electrodes have (meta)stable hosts already available in MP, like $FePO_4$ in olivine $LiFePO_4$, other frameworks, such as the double-perovskite $Ca_2FeMoO_6$, have an unstable host ($FeMoO_6$) that is absent from the MP database. Thus, if a (meta)stable host exists, it can possibly co-exist with an intercalated state of the electrode at a given average voltage, such as $FePO_4$ co-existing with $LiFePO_4$ at an average voltage of ∼0.46 V vs. SHE (see **Figure S5a**) [95]. Therefore, to

evaluate intercalation voltages across materials, we query the fully deintercalated structure for each seawater (meta)stable intercalated structure from MP and subsequently evaluate the seawater metastability of the host. Note that a given intercalated structure can be identified as being similar to several deintercalated structures (including structures with minor distortions and partial deintercalation) and vice-versa, implying the need to identify common host frameworks across multiple structures (see **Section 2.6** for details).

After identifying all the topotactic (de)intercalated states of an electrode host, we determine the states that can thermodynamically co-exist at a constant voltage using pseudo-binary convex hulls, where the composition of the electroactive ion is varied across the (de)intercalated structures. Using DFT-calculated energies from the MP, we construct a 0 K pseudo-binary hull for each combination of a host and an electroactive ion. Note that the pseudo-binary hulls are used solely to determine possible coexisting phases, not to reassess the seawater (meta)stability (see **Figure S6** for a schematic and further explanation).

Specifically, only phases connected by a facet (or a tie-line) of the pseudo-binary convex hull are thermodynamically allowed to coexist and we compute the average intercalation voltage (versus SHE) for each pair of coexisting phases. If the calculated voltage lies within the seawater metastability window, we check the metastability of both the coexisting phases and screen for pairs that remain metastable across the entire 7-8.5 seawater pH window at their intercalation voltage (see the $Li_2VCu(PO_4)_2$-$VCu(PO_4)_2$ example in **Figure 3c**). If the seawater metastability areas of two phases on a facet do not overlap or if the calculated voltage of a coexisting pair falls outside the overlapping region of metastability of the individual phases (see example in **Figure S6c1, c2**), the corresponding intercalated phase is removed from the pseudo-binary hull and the hull is recomputed. We repeat this procedure recursively until all suitable candidate pairs, i.e., intercalated-deintercalated structure pairs with overlapped metastability region and voltage within the seawater stability window, of a given host are identified or all structures mapped to a host are exhausted.

It is important to note that under operating electrochemical conditions, operating voltages for electrodes can deviate away from our predicted values due to overpotentials as well as any phase transitions in the electrode material. Hence, it is necessary that a candidate electrode is stable over a wider range of potentials around the computed voltage. For example, olivine-$LiFePO_4$ exhibits an average voltage of 0.46 V vs. SHE, which is approximately equidistant from both the H and O evolution lines within the seawater stability window (**Figure S5a**). Additionally, the metastability regions of olivine-$LiFePO_4$ and its deintercalated-$FePO_4$ states overlap over 88% of the seawater metastability window (**Figure S5a**), enabling the coexisting phases to accommodate large overpotentials. Thus, the percentage overlap of an electrode's metastability region with the seawater metastability window is an important metric to quantify the utility of an electrode under operating conditions.

We use a percentage metastability overlap metric of $\geq$80%, since this is similar to the overlap exhibited by olivine-$LiFePO_4$ ($\sim$88%, **Figure S5a**), to screen for electrode candidates that are metastable and exhibit a voltage within the seawater stability window. Note that our metastability overlap metric requires the area of intersection of the metastable regions of both the intercalated and deintercalated phases to constitute $\geq$80% of the seawater stability window. For instance, the $Li_2VCu(PO_4)_2$-$VCu(PO_4)_2$ pair in **Figure 3c** exhibits an overlap of the metastability regions of the individual phases and an average intercalation voltage of $\sim$0.20 V vs. SHE that is within the seawater stability window. However, the pair's metastability overlap constitutes <80% of the overall seawater stability window and hence is not considered a candidate for further analysis.

In summary, in this step, we screen for pairs of deintercalated-intercalated structures with *i*) an intersecting (or overlapping) region of metastability, *ii*) an average intercalation voltage that lies within the

intersecting metastability region across the entire 7-8.5 pH range, and *iii*) the intersecting metastability area occupying at least 80% of the seawater stability window.

## 2.6 Comparing framework structures

To map and visualize all unique intercalated-deintercalated combinations with similar hosts for voltage and metastability overlap calculations (**Section 2.5**), we constructed computational graphs, as shown in **Figure 3b** and **d**. Circular and hexagonal nodes in our graphs represent theoretical and experimental structures, respectively, with the color of a node representing the electroactive ion associated with the host. Gray colored nodes typically reflect deintercalated hosts that can accommodate multiple types of cations. Edges in our graphs connect structures with similar underlying hosts, with the type of the edge (solid or dashed and blue or gray) encoding information on the metastability of the connected nodes (see **Figure 3d**). We use `pymatgen`'s `StructureMatcher` module, with its default tolerances, to identify whether two underlying hosts are similar or not. Thus, each graph is a collection of one or more interconnected nodes, with each node representing various intercalated states of a host and every pair of connected nodes signifying a possible topotactic intercalated-deintercalated combination.

As an example, **Figure 3b** shows the graph for a polymorph of $CoSiO_4$ host (with a MP ID of mp-25268), comprising four compositions – $CoSiO_4$, $LiCoSiO_4$, $Li_2CoSiO_4$, and $Li_3CoSiO_4$. The edges among the $CoSiO_4$, $LiCoSiO_4$, and $Li_3CoSiO_4$ nodes indicate that these three structures share similar underlying $CoSiO_4$ hosts (i.e., the structures are similar if all Li are removed from each structure). Notably, the $Li_2CoSiO_4$ node connects to $LiCoSiO_4$ and $Li_3CoSiO_4$ but not to $CoSiO_4$, which can be attributed to deviations in the $CoSiO_4$ host structure associated with $Li_2CoSiO_4$ that does not match well with the pure $CoSiO_4$ host, per the default tolerances of the `StructureMatcher` module. We interpret this to mean that Li insertion into $CoSiO_4$ generally distorts the pure $CoSiO_4$ host, with the distortion at $Li_2CoSiO_4$ being particularly strong. Although every node in this graph (**Figure 3b**) is not connected to every other node, their presence in a single graph demonstrates that they share a common host, with distortions arising from the (de)intercalation of the electroactive ion. Thus, we classify all structures being part of a graph to exhibit a similar underlying host, as long as a given structure shares at least one edge to another structure in the graph.

Upon identifying electrodes with suitable operating voltages and high metastability area overlap in **Section 2.5**, we compare the hosts across different working ions to distinguish the structures that intercalate a single ion (for ion recovery) from those that can intercalate multiple ions (for desalination). Specifically, we construct computational graphs for all structures across the five electroactive ions, as shown for the example of olivine-$FePO_4$ in **Figure 3d**. Physically, each graph (that contain a cluster of interconnected nodes) corresponds to a single host structure that is capable of intercalating one or multiple cations, thus encoding the ion-selectivity information. Importantly, solid blue edges in our graphs (**Figure 3d**) indicate that the two nodes are not only seawater metastable at their (de)intercalation voltage but also exhibit an interesecting metastability area that occupies $\geq$80% of the seawater stability window. Thus, we enlist all nodes (i.e., structures) that are connected by solid blue edges as the most promising candidates for ion capture and include the information on whether a given host is selective to a specific cation or it can intercalate multiple cations as well.

# 3 Results

## 3.1 Screening statistics

In total, we evaluate the seawater metastability of 12,536 Li, 3,598 Mg, 1,344 Ca, 1,783 Na and 1,153 K intercalation electrodes, as queried from MP (cyan bars in **Figure 2b**), with most of the queried electrodes, namely 10,131 Li, 2,437 Mg, 780 Ca, 1,185 Na and 559 K, being metastable in seawater at some pH and applied potential (purple bars). Subsequently, screening for intercalation-deintercalation pairs that are metastable at their intercalation voltage reduces the number of candidates significantly, yielding possibly 754 Li, 195 Mg, 95 Ca, 68 Na, and 21 K hosts, as summarized by the gray circles in the Venn diagrams of **Figure 4**. Application of the screening criteria, as developed in **Sections 2.5** and **2.6**, causes further reductions in the number of possible electrodes. For instance, requiring the intercalation-deintercalation pairs to be metastable at their intercalation voltage, across the entire 7-8.5 seawater pH range, and ensuring an intersecting area that occupies at least 80% of the seawater stability window (as outlined in **Section 2.5**) results in a total of only 69 Li, 13 Mg, 10 Ca, 10 Na, and 3 K hosts, displayed as yellow circles in **Figure 4**. Thus, we deem all the hosts constituting the yellow circles in **Figure 4** to be potential candidates for electrochemical ion capture. Finally, there are 8 Li, 4 Mg, 4 Ca, 7 Na, and 0 K hosts that have at least one experimental phase among the intercalated-deintercalated pairs (green circles in **Figure 4**), highlighting the strongest set of candidates for experimental trials of ion capture. The final list of experimentally known candidates, alongside the most promising theoretical candidates are compiled in **Table 1** and in the sections below.

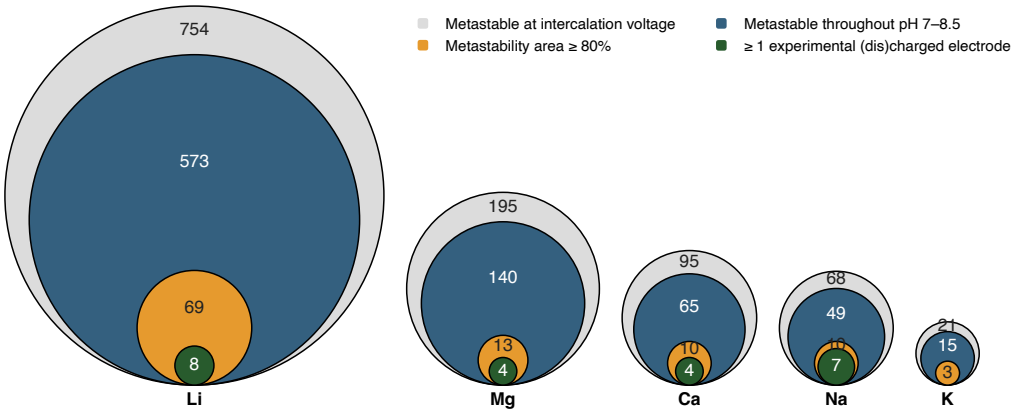



Figure 4: Venn diagrams showing the reduction in the number of candidate electrodes with sequential screening. Gray circles indicate the number of intercalation-deintercalation pairs that are metastable at their operating voltage, while blue circles enumerate pairs that are metastable across the entire 7-8.5 seawater pH window. Yellow circles indicate the number of pairs which exhibit an intersecting metastability area that occupies more than 80% of the seawater stability window. Green circles signify the subset of pairs that have at least one experimentally known structure.

## 3.2 Ion selectivity statistics

The Venn diagrams in **Figure 4** do not show the intersection of the sets across the electroactive ions considered, i.e., the statistics represent those for a single electroactive ion and do not include ionic selectivity. Therefore, all structures within the gray sets of **Figure 4** are nodes in our computational graphs (see the

example in **Figure 3d**). The connectivity of edges in a graph encodes the ion-selectivity information, thus motivating our use of computational graphs in this work. Another reason for the use of graphs is to overcome the limitations of finite and default tolerances that are often used in matching structures/hosts, since there are no universal set of tolerances that work well across different structural groups and their types of distortions. Importantly, we compile the cases of hosts belonging to the gray sets of **Figure 4** that can intercalate single or multiple cations via our graph constructions and depict the statistics in **Figure 5**.

Graphs (or hosts) that can intercalate only one cation are depicted as having nodes of the same color, namely, red, blue, green, yellow, and violet colors for Li, Mg, Ca, Na, and K, respectively, in **Figure 5a**. Most of the hosts that intercalate only a single cation are Li-selective (587 hosts, **Figure 5a**), reflecting the larger volume of available Li data, followed by 94 Mg, 27 Ca, 11 Na, and 8 K selective hosts. Graphs displaying nodes of multiple colors, as shown in panels b, c, and d of **Figure 5**, represent hosts that can intercalate more than one cation. Among such hosts, we identify 115 frameworks that intercalate two cations (**Figure 5c**), 28 hosts that intercalate three cations (**Figure 5d**), and five hosts that intercalate four cations (**Figure 5b**). Notably, our screening identifies no host structure that can intercalate all five electroactive cations considered in this work, indicating that there is no perfect electrode candidate for desalination.

### 3.3 Ion-selective and non-selective electrodes

While the collection of graphs in **Figure 5** show numerous ion-selective/non-selective hosts, we are interested in the most promising among them, as represented by the frameworks in the yellow or green sets of **Figure 4**. Hence, we compile the set of candidates that we identify as most promising across all electroactive cations and for both ion-selective and non-selective use cases in **Figure 6**. The most deintercalated state of the host (and its MP ID) is labeled along the horizontal axis for the case of ion-selective (panel a) and non-selective (panel b) scenarios in **Figure 6**, with the vertical axis in both panels indicating the intercalation voltage. Note that each voltage value corresponds to the coexistence of an intercalated and a deintercalated phase, with circular and hexagonal shapes indicating cases with only theoretical structures and at least one experimental structure in a given pair, respectively. Color coding in **Figure 6a** and **b** is identical to **Figure 5**, with the horizontal blue dashed lines representing the narrowest voltage window of seawater stability across the 7-8.5 pH range.

Among the screened metastable hosts constituting the yellow sets of **Figure 4**, 66 Li, four Mg, three Ca, three Na, and two K hosts intercalate only a single ion and qualify as ion-selective electrodes. Given the large number of Li-selective electrodes in the yellow set, we considered the Li-selective electrodes in the experimental (green) subset to be the most promising, which include $LiFeP_2O_7$ (mp-19294, **Figure 6c**), $Fe_2(PO_4)_3$ (mp-26412, **Figure 6d**) and $Fe_2(MoO_4)_3$ (mp-21925, **Figure 6e**). Among the screened ion-selective hosts for Mg, Ca, and Na, we identify two hosts in the green subset for each cation, namely, $NbCoO_4$ (mp-31518), and $TiFe_2O_5$ (mp-35482) for Mg, $Ca_3Co_2(Si_2O_7)_2$ (mp-1256217), and $CaFeMoO_6$ (mp-1368738) for Ca, and $Fe_7(PO_4)_6$ (mp-510351), and $NaFe_3(PO_4)_3$ (mp-556692) for Na. Notably, all candidates identified as promising K-selective are theoretical hosts.

**Figure 6b** compiles the promising candidate hosts (i.e., from the yellow sets of **Figure 4**) for intercalating two cations (blue shaded region), three cations (pink shaded), and four cations (green shaded) simultaneously, thus representing the shortlisted candidates for non-selective ion capture. For the case of hosts that can capture Li and other cation(s), we prioritized the listing of experimentally known hosts in **Figure 6b**, similar to **Figure 6a**. Faded symbols in **Figure 6b** indicate that the intercalated-deintercalated pair involving the specific electroactive ion is not seawater metastable during operation, while the hatched symbols indicate

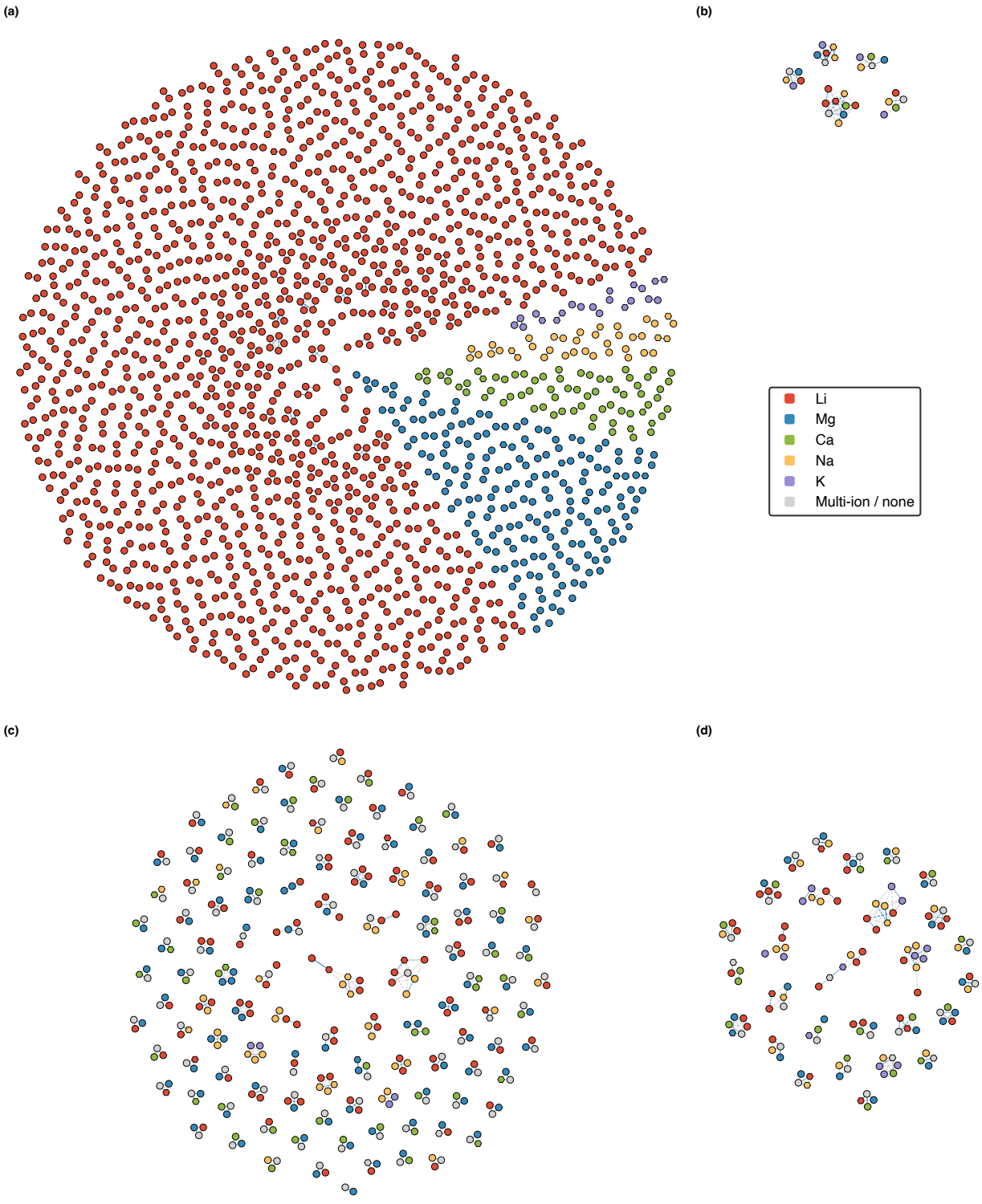



Figure 5: Graphs of all hosts that can intercalate (a) one, (b) four, (c) two, and (d) three distinct cations, corresponding to a total of 859, 5, 115, and 28 hosts, respectively.

pairs that have an intersection area that occupies 70% to 80% of the seawater stability window across the full 7-8.5 pH range. In the case of non-selective hosts, we do obtain frameworks that are not as metastable

for specific electroactive ions during our screening process (i.e., the faded and hatched symbols) since all structures across different electroactive ions that are identified as similar belong to the same graph. While we don't expect hosts indicated by faded symbols to be promising for the specific cation, hosts highlighted by hatched symbols may still be relevant for experimental trials involving stricter potential controls.

Importantly, several hosts in **Figure 6b** show a 'small' difference (<0.1 V) in the intercalation voltage among different cations and are hence likely to intercalate multiple ions at the same overpotential experimentally. Examples include the different polymorphs of $FePO_4$ (mp-25303, mp-752872, and mp-776288) that intercalate two cations, the Ca-Mg intercalating $Fe_2(MoO_4)_3$ (mp-1042928), the Na-Li intercalation in $Fe(PO_3)_3$ (mp-25310) and $NaCoPCO_7$ (mp-1101670), the Na-K intercalation in $LiFePCO_7$ (mp-1176697), and Mg-K intercalation in olivine-$FePO_4$ (mp-20361). Other hosts in **Figure 6b** exhibit voltage differences that are >0.1 V among the intercalating cations, indicating that these electrodes may be better used in selectively intercalating a specific cation using potentiostatic conditions.

## 3.4 Shortlisted ion-selective hosts

In this section, we provide detailed descriptions of the host structures that are identified as most promising ion-selective hosts for each electroactive ion considered and compiled in **Figure 6a**. For non-Li intercalating hosts, we provide descriptions of theoretical hosts that we have identified with our workflow, which are potential candidates as well. The constructed seawater Pourbaix diagrams for all candidates described here are compiled in **Figure S7** of the SI, while the corresponding computational graphs are shown in **Figure S11**.

### 3.4.1 Li-selective

$LiFeP_2O_7$ (mp-19294, **Figure 6c**) belongs to the pyrophosphate [62] family of compounds with a monoclinic $P2_1$ spacegroup, tetrahedrally coordinated $PO_4$ and octahedrally coordinated $FeO_6$. Each $PO_4$ tetrahedron shares one corner with another $PO_4$ tetrahedron, forming $P_2O_7$ units. While each $PO_4$ shares three corners with three different $FeO_6$ octahedra, each $FeO_6$ is connected to five different $P_2O_7$ groups, where one of the $P_2O_7$ groups acts as a chelating sequence around the Fe [96, 97], resulting in $FeP_2O_7$ units that create open channels for Li intercalation. $LiFeP_2O_7$ forms as the fully deintercalated phase experimentally with Fe in the +3 oxidation state. Li intercalation reduces the Fe to +2 and yields $Li_{1+x}FeP_2O_7$, which has been experimentally reported for $0 \leq x \leq 0.8$ [96]. However, at $x = 1$, the topotactic $P2_1$ intercalated phase ($Li_2FeP_2O_7$, mp-779056) remains a theoretical structure, albeit with the intersecting metastability area occuping 88% of the seawater stability window (**Figure S7d**). Our estimated intercalation voltage (0.02 V vs. SHE or 3.06 V vs. Li) for the $LiFeP_2O_7$—$Li_2FeP_2O_7$ pair is in close agreement with the experimentally reported two-phase plateau of 2.92 V vs. Li [96, 97].

$Li_3Fe_2(PO_4)_3$ (mp-25993) has a monoclinic anti-NASICON (Na superionic conductor) structure in the $P2_1/c$ spacegroup, consisting of $PO_4$ tetrahedra and two crystallographically distinct $FeO_6$ octahedra. Each $FeO_6$ octahedra shares all its edges with $PO_4$ tetrahedra and vice versa, leading to a three dimensional framework allowing for three distinct Li sites with different coordination environments. $Li_3Fe_2(PO_4)_3$ has Fe in its +3 oxidation state and experiments report two distinct voltage plateaus upon intercalation, resulting in $Li_4Fe_2(PO_4)_3$ and $Li_5Fe_2(PO_4)_3$ [98]. Note that $Li_3Fe_2(PO_4)_3$ shares the same host lattice as $Fe_2(PO_4)_3$ (mp-26412, **Figure 6d**), which is the most deintercalated composition in the graph and is available in MP as well, explaining its listing in **Figure 6a**. However, $Fe_2(PO_4)_3$ is not seawater stable and only $Li_3Fe_2(PO_4)_3$ - $Li_5Fe_2(PO_4)_3$ and $Li_2Fe_2(PO_4)_3$ - $Li_5Fe_2(PO_4)_3$ pairs are metastable with an intersecting area of over 80%

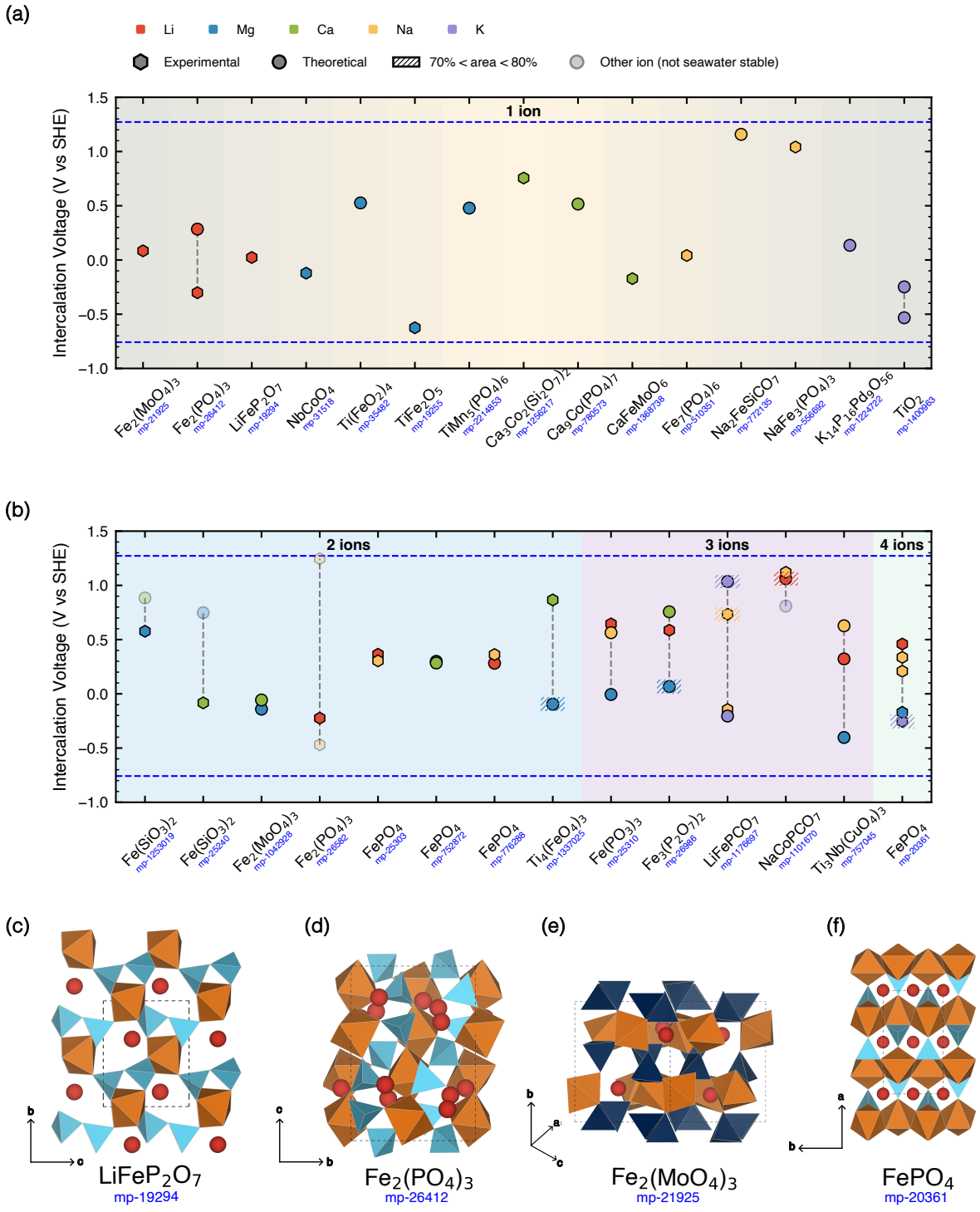



Figure 6: Intercalation voltages of the shortlisted (a) ion-selective and (b) non-selective intercalating hosts. (c)-(e) Structures of promising Li-selective electrodes where the light blue tetrahedra, orange octahedra, and dark blue tetrahedra indicate $PO_4$, $FeO_6$, and $MoO_4$, respectively. (f) Olivine-$FePO_4$ with the same colour scheme as panels (c)-(d). Red spheres in panels (c)-(e) show sites occupied by electroactive cations in the lattice.

of the seawater stability window (see **Figure S7b1,b2**). Here, we consider the $Li_3Fe_2(PO_4)_3$ - $Li_5Fe_2(PO_4)_3$ pair, with a voltage of $-0.3$ V vs. SHE, to be the most promising since this pair has been experimentally reported [98]. Also, $Li_3Fe_2(PO_4)_3$ and $FeP_2O7$ have been explored as an intercalation electrodes in aqueous LIBs [99].

$Fe_2(MoO_4)_3$ (mp-21925, **Figure 6e**) exhibits an orthorhombic *Pbcn* spacegroup containing $FeO_6$ octahedra and $MoO_4$ tetrahedra that share their corners with distinct $MoO_4$ and $FeO_6$ groups, respectively. As a result, the framework forms intercalation sites that are interconnected in all three dimensions. Topotactic lithiation of $Fe_2(MoO_4)_3$ leads to the orthorhombic $Li_2Fe_2(MoO_4)_3$ (mp-21778) which has also been experimentally reported alongside the $Fe_2(MoO_4)_3$ phase [100]. In the deintercalated phase, Mo and Fe are in oxidation states +6 and +3, respectively, with Fe undergoing reduction to the +2 oxidation state upon Li intercalation. The constructed seawater Pourbaix diagram of this system is shown in **Figure S7a**.

### 3.4.2 Mg-selective

The most deintercalated versions of the Mg-selective hosts are summarized in panels a-d of **Figure 7** and their corresponding seawater Pourbaix diagrams are compiled in **Figure S7d-g**. The experimentally observed hosts that are Mg-selective include $NbCoO_4$ (mp-31518, **Figure 7a**) and $TiFe_2O_5$ (mp-19255, **Figure 7b**). $NbCoO_4$ is a monoclinic structure ($C2/m$ spacegroup [101]), which forms the theoretical $Mg_{1/2}NbCoO_4$ (mp-2219413) upon Mg intercalation. The deintercalated $NbCoO_4$ phase contains Nb and Co in the oxidation states +5 and +3, respectively, forming a network of edge sharing and corner sharing $NbO_6$ and $CoO_6$ octahedra. $Mg^{2+}$ intercalation results in the reduction of Co only to its oxidation +2, which is accompanied by distortions in the $CoO_6$ octahedra. Mg occupies two symmetrically distinct triangular bipyramidal voids in the host. Similar to $NbCoO_4$, $TiFe_2O_5$ is also monoclinic ($C2/c$ spacegroup [102]) and forms the theoretical $Mg_{1/2}TiFe_2O_5$ structure (mp-2229085, $P1$ spacegroup) upon Mg intercalation. The deintercalated structure consists of edge- and corner-sharing $FeO_6$ octahedra that are intertwined with corner-sharing $TiO_6$ octahedra, with Ti and Fe in their +4 and +3 oxidation states, respectively. With Mg intercalation, Fe reduces to its +2 oxidation state alongside distortions both in the $FeO_6$ and $TiO_6$ octahedra.

There are two theoretical Mg-selective candidates that we identify in our workflow, namely, $TiMn_5(PO_4)_6$ (mp-2214853, **Figure 7c**) and $Ti(FeO_2)_4$ (mp-35482, **Figure 7d**). $MgTiMn_5(PO_4)_6$ (mp-2216952), which forms upon Mg intercalation in $TiMn_5(PO_4)_6$ shares the same triclinic $P1$ spacegroup with the deintercalated host, which contains $TiO_6$ octahedra, $MnO_6$ octahedra and $PO_4$ tetrahedra. Mg intercalation into the structure is expected to reduce $Mn^{3+}$ to $Mn^{2+}$ with Ti remaining in its +4 oxidation state. However, we do not expect the $TiMn_5(PO_4)_6$ to be a feasible candidate since the structure is relatively 'closed' making it unlikely to facilitate diffusion of $Mg^{2+}$. In the case of $Ti(FeO_2)_4$, the structure is an ordered, monoclinic ($C2/m$ spacegroup) representation of an experimentally reported defective spinel structure that contains both Ti and Fe across tetrahedral and octahedral sites of the lattice [103]. Specifically, $Ti(FeO_2)_4$ has $Ti^{4+}$ occupying only the octahedral sites of the spinel while $Fe^{3+}$ occupies both tetrahedral and octahedral sites. Mg intercalation yields $MgTi(FeO_2)_4$ (mp-2228463, $C2/m$), resulting in the reduction of $Fe^{3+}$ and the occupation of Mg within the octahedral voids. Given that spinels generally provide reasonable diffusivity for $Mg^{2+}$ [104, 105], we expect $Ti(FeO_2)_4$ to be a potential candidate for experimental trials.

### 3.4.3 Ca-selective

There are three candidate hosts that are Ca-selective per our workflow, which are compiled in panels e-g in **Figure 7** with their corresponding seawater Pourbaix diagrams listed in **Figure S7h-j**. Among these

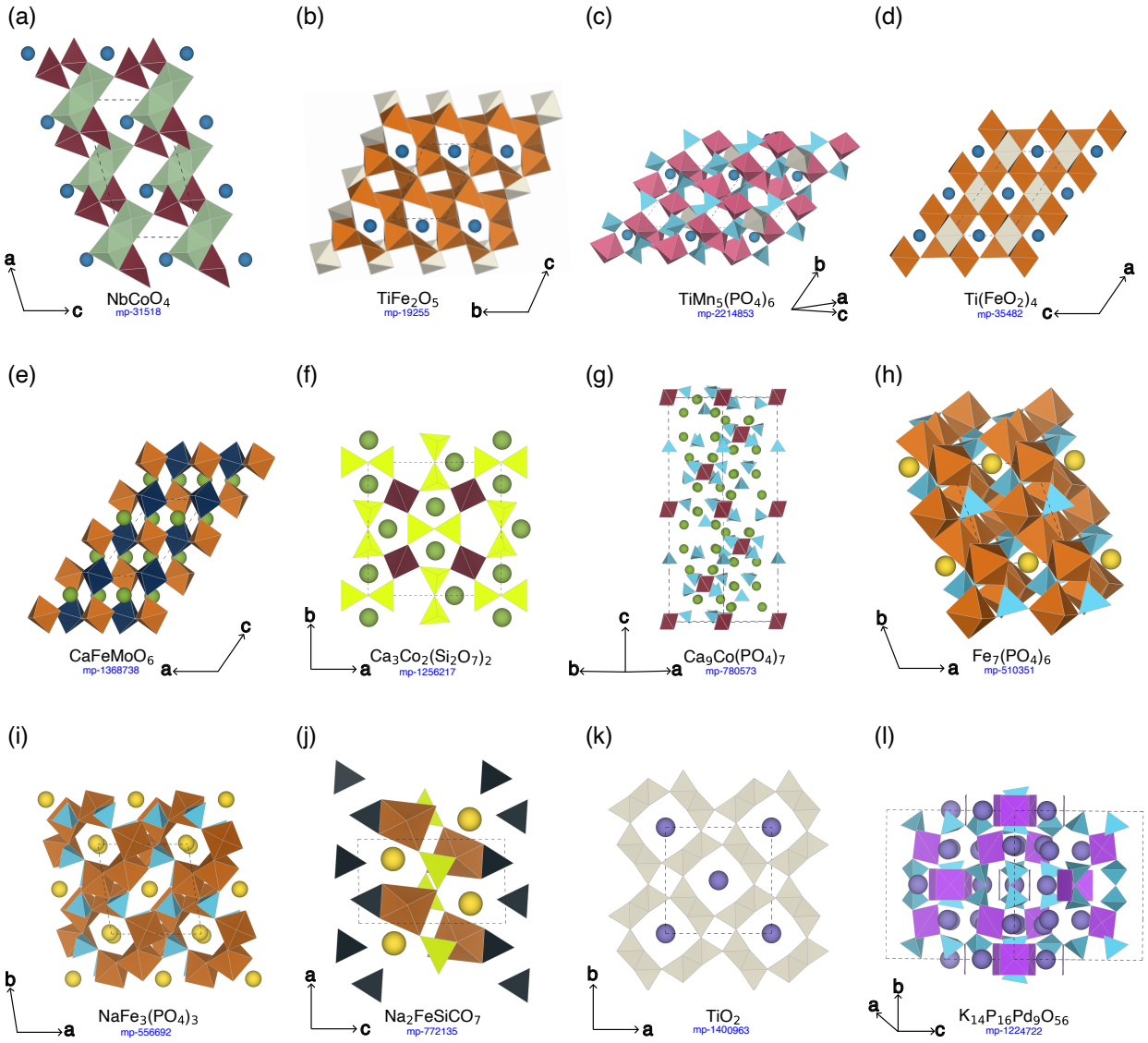



Figure 7: (a)-(d) Mg-selective electrodes, where the blue spheres indicate possible $Mg^{2+}$ sites. (e)-(g) Ca-selective electrodes, where the green spheres indicate $Ca^{2+}$. (h)-(j) Na-selective electrodes, with yellow spheres representing $Na^{+}$. (k)-(l) K-selective electrodes, with purple spheres representing $K^{+}$. The chemical formulae and MP ID below each panel corresponds to the most de-intercalated state represented in the corresponding graph (see **Figure S11**). The dashed lines in each panel show the conventional unit cell. Following is the color scheme of the polyhedra: orange – $FeO_6$ octahedra/$FeO_5$ trigonal bipyramids in panels (b), (d), (e), (h)-(j); light-blue – $PO_4$ tetraheadra in (c), (g)-(i), (l); light-gray – $TiO_6$ octahedra in (b)-(d), (k); dark-brown – $CoO_6$ octahedra in (a), (f), (g); neon-green – $SiO_4$ tetrahedra in (f), (j); olive-green – $NbO_6$ octahedra in (a); pink – $MnO_6$ octahedra in (c); dark-blue – $MoO_6$ octahedra in (e); dark-gray – trigonal planar $CO_3$ in (j); and bright-purple – $PdO_6$ octahedra/$PdO_5$ square pyramids in (l).

$Ca_2FeMoO_6$ (mp-18783) and $Ca_2CoSi_2O_7$ (mp-18786) have been experimentally reported. $Ca_2FeMoO_6$ is a monoclinic double perovskite with $P2_1/n$ symmetry containing alternating $FeO_6$ and $MoO_6$ octahedra which are tilted to optimize coordination around the $Ca^{2+}$ that occupies the 'A' site of a $ABO_3$ perovskite [106]. The most deintercalaed version of $Ca_2FeMoO_6$ found in MP is the $CaFeMoO_6$ (mp-1323783, **Figure 7e**), with another deintercalated structure, $Ca_{3/2}FeMoO_6$ (mp-1368738) are also found in MP. However, we find

only the $Ca_{3/2}FeMoO_6$-$Ca_2FeMoO_6$ pair to be seawater metastable.

The other experimental phase, $Ca_2CoSi_2O_7$ is a tetragonal structure ($P\bar{4}2_1m$ symmetry) with corner-sharing $CoO_4$ tetrahedra and $Si_2O_7$ pyrosilicate dimers [107–111]. The most deintercalated version of this host in MP is $Ca_{3/2}CoSi_2O_7$ (listed as $Ca_3Co_2(Si_2O_7)_2$, mp-1256217, **Figure 7f**). Here Si remains in the +4 oxidation state and Co acts as the redox-active element with +2 and +3 oxidation states in the intercalated and deintercalated states, respectively. $Ca_9Co(PO_4)_7$ (mp-780573, **Figure 7g**) is a theoretical deintercalated phase with a theoretical intercalated $Ca_{9.5}Co(PO_4)_7$ (mp-1228767) phase, where both structures exhibit trigonal ($R3c$) symmetry. The deintercalated phase contains Co in the +3 oxidation state forming $CoO_6$ octahedra, which reduce to $Co^{2+}$ upon Ca intercalation.

### 3.4.4 Na-selective

The most deintercalated versions of the Na-selective hosts are summarized in panels h-j of **Figure 7**, with their seawater Pourbaix diagrams given in **Figure S7k-m**. Note that Na-selective hosts may still be useful for desalination applications, since $Na^+$ is the most abundant and critical cation to be removed from seawater. Among the candidate hosts, $Fe_7(PO_4)_6$ (mp-510351, **Figure 7h**) is an experimentally reported [112–115] triclinic structure with a $P\bar{1}$ spacegroup. The framework contains infinite chains of edge-sharing $FeO_6$ octahedra and edge-sharing $FeO_5$ trigonal bipyramids, which are linked by a set of corner-sharing $FeO_6$ octahedra and $PO_4$ tetrahedra. In the completely deintercalated structure, Fe exists in both its +2 and +3 oxidation states in a 3:4 ratio across all Fe-containing polyhedra [116–118]. Addition of Na leads to an intercalated structure where the $Fe^{2+}$:$Fe^{3+}$ ratio increases to approximately 4:3, resulting in the formation of the experimentally reported $NaFe_7(PO_4)_6$ (mp-1205097) $P\bar{1}$ structure [115, 116]. Further optimization of the Na intercalation process can potentially enable more Na atoms to be captured by the structure, given that all Fe atoms are not fully reduced in $NaFe_7(PO_4)_6$.

$NaFe_3(PO_4)_3$ (mp-556692, **Figure 7i**) and its intercalated phase $Na_2Fe_3(PO_4)_3$ (mp-558822) both are experimentally reported alluaudite type structures [119, 120] with monoclinic $C2/c$ spacegroup. The framework contains zigzag chains of edge-sharing $FeO_6$ octahedra with $PO_4$ tetrahedra forming bridges between the Fe-O chains via corner-sharing, leading to two distinct one dimensional Na diffusion pathways, typical of alluaudites [63]. While $NaFe_3(PO_4)_3$ has been reported only as a minor hydrothermal by-product [120], $Na_{2-x}Fe_3(PO_4)_3$ ($x \approx 0$ to 0.5) is readily synthesizable via various routes, and has been used as a Na-ion cathode with non-aqueous electrolytes [121–124]. We estimate that sodiation of $NaFe_3(PO_4)_3$ to $Na_2Fe_3(PO_4)_3$, leading to reduction of $Fe^{3+}$ to $Fe^{2+}$, occurs at 1.04 V vs. SHE (3.75 V vs. $Na/Na^+$), which is ∼0.7-1.0 V above the experimentally reported intercalation voltages [122, 123]. We attribute this discrepancy in the intercalation voltage to the different Na site occupancy of the $NaFe_3(PO_4)_3$ structure in MP [120], versus experimental $Na_{2-x}Fe_3(PO_4)_3$ structures [122, 123].

$Na_3Fe(CO_3)(SiO_4)$ (documented as $Na_3FeSiCO_7$, mp-771204) is a monoclinic mixed-polyanion silicate carbonate with $P2_1/m$ symmetry, similar to the sidorenkite $Na_3Mn(PO_4)(CO_3)$ structure [125–127]. It contains $FeO_6$ octahedra, sharing four corners with $SiO_4$ tetrahedra and one edge with trigonal-planar $CO_3$. The most deintercalated version of $Na_3Fe(CO_3)(SiO_4)$ found in MP is $Na_2Fe(CO_3)(SiO_4)$ (mp-772135), as shown in **Figure 7j**. Unlike a phosphate carbonate (e.g., $Na_xFe(PO_4)(CO_3)$), where the redox-active Fe is either in the +2 (intercalated) or +3 (deintercalated) oxidation states, replacing $Si^{4+}$ with $P^{5+}$ increases the Fe oxidation state to +3 in the sodiated state, and +4 in the desodiated state [128]. Both the sodiated and desodiated silicate carbonates are theoretical structures, and Hautier et. al.'s [128] high-throughput computational study reported $Na_3Fe(CO_3)(SiO_4)$ (where Fe is in the +3 state) to be stable at 0 K. However,

due to the presence of Fe in its +4 oxidation state with sodium removal, synthesis of this phase may be challenging.

#### 3.4.5 K-selective

Both the shortlisted K-selective electrodes are theoretical, namely, $TiO_2$ (mp-1400963, **Figure 7k**) and $K_{14}P_{16}Pd_9O_{56}$ (mp-1224722, **Figure 7l**), with the corresponding seawater Pourbaix diagrams shown in **Figure S7n-o2**. The $P_{16}Pd_9O_{56}$ host contains all the Pd in a planar geometry, bonded to four $O^{2-}$, with $PO_4$ tetrahedra connecting three different $PdO_4$ units, resulting an interconnnected network of prismatic sites that are occupied by $K^+$. Upon K intercalation, there are two possible compositions with the host per MP, namely, $K_{14}P_{16}Pd_9O_{56}$ (mp-1224722) and $K_{15}P_{16}Pd_9O_{56}$ (mp-1212473). We expect the $P_{16}Pd_9O_{56}$ host to be challenging to realise experimentally, owing to the high cost of Pd.

The $TiO_2$ host is tetragonal ($I4/m$ spacegroup) with a hollandite $MnO_2$-like structure [129], and $TiO_6$ forming a mixture of corner- and edge-sharing octahedra that allow for one dimensional channels that accommodate $K^+$ within prismatic voids. Upon K intercalation, the $TiO_2$ host can form two intercalated structures, namely, $K_{1/16}TiO_2$ (mp-757418) and $K_{1/6}TiO_2$ (mp-765472), per MP. Although MP flags all three structures as theoretical, they correspond closely to the experimentally reported $TiO_2$, $K_{0.06}TiO_2$ and $K_{0.17}TiO_2$ [130, 131]. While Li intercalates into several $TiO_2$ polymorphs ( [132, 133]), the experimentally reported $Li^+$ insertion voltage into the hollandite $TiO_2$ lies below the seawater stability window [134]. This unfavorable experimental Li-intercalation voltage, combined with the fact that MP does not contain any Li-intercalated hollandite-$TiO_2$ structures, indicates that hollandite-$TiO_2$ is likely to be selective towards $K^+$ in seawater conditions.

### 3.5 Shortlisted non-selective hosts

In this section, we provide detailed descriptions of the host structures that are identified as most promising non-selective hosts (i.e., capable of intercalating multiple cations), as compiled in **Figures 6a** and **S12**. The constructed seawater Pourbaix diagrams for all candidates described here are compiled in **Figures S8-S10** of the SI, while the corresponding computational graphs are shown in **Figures S13** and **3d**.

#### 3.5.1 Olivine-$FePO_4$

While our workflow does not identify the ideal desalination electrode that can intercalate all five electroactive ions considered, the closest to the ideal candidate that we identify is olivine-$FePO_4$ (mp-20361, **Figure 6f**). While we do identify layered-$CoO_2$ (mp-1275937) and layered-$FeO_2$ (mp-25236) to also intercalate four out of five cations considered in this work, both hosts do not exhibit metastability regions that occupy near 80% of the seawater stability window and hence are not feasible candidates. In terms of structure, olivine-$FePO_4$ contains parallel planes of equivalent corner-sharing $FeO_6$ octahedra, with Fe in its +3 oxidation state, that are bridged by $PO_4$ tetrahedra. The resulting framework provides one dimensional diffusion channels for the intercalating ions, with the reduction of Fe from +3 to +2 upon intercalation. We expect the $FePO_4$ to intercalate Li, Mg, Na, and K under seawater conditions, with the associated Pourbaix diagrams compiled in **Figure S10** and the computational graph in **Figure 3d**.

Li and Na intercalation in olivine-$FePO_4$ are well documented with their reported intercalation voltages closely matching our predicted values of 0.46 and 0.29 V vs. SHE, respectively [22, 135–139]. While Mg

and K intercalated structures in MP are theoretical, there have been experimental reports of Mg [140] and K [141] intercalation in $FePO_4$ in aqueous media, with K intercalation reported to be irreversible due to amorphization caused by large lattice strains. We do show that intercalation of K in $FePO_4$, although possible, is not as (meta)stable as the intercalation of Li, Na or Mg, as indicated by the lower intersecting metastability area (∼74% of the seawater stability window) signifying the susceptibility of the system to decompose under high overpotentials. Also, experiments highlight limited capacity for intercalation of Mg in $FePO_4$, which agrees with our observation as well, given that the most intercalated metastable Mg phase is $Mg_{1/4}FePO_4$ that has Mg occupying only one-quarter of all possible intercalation sites. Interestingly, while there have been experimental reports of possible Ca intercalation in olivine-$FePO_4$ [142], there are no Ca containing olivine structures in MP, resulting in a lack of rigorous evaluation of Ca intercalation in olivine-$FePO_4$.

### 3.5.2 Multi-cation intercalating hosts

Hosts that can intercalate multiple cations simultaneously, such as two or three from the five cations considered in this work, can have use cases for different applications. For instance, $Na^+$ remains the critical entity to remove in any desalination process, so hosts that can remove $Na^+$ efficiently with any other cation can be useful for desalination workflows. Similarly, electrodes that can simultaneously remove $Mg^{2+}$ and $Ca^{2+}$ can be used for water softening applications. Moreover, potentiostatic techniques can be used to make non-selective hosts selective to a specific cation, if the intercalation voltages of the different cations are sufficiently far apart (>0.1 V, **Figure 6b**). Thus, similar intercalation voltages facilitate hosts to be non-selective while distinct intercalation voltages enable hosts to be selective. Moreover, intercalating multiple ions when their potentials are significantly separated may by challenging, since the reaction kinetics decay exponentially with the overpotential. Note that the similarities or differences in intercalation voltages with distinct cations in a structure are determined by two factors: *i*) relative (in)stability of the intercalated and deintercalated compositions (which can be modified with doping for instance), and *ii*) differences in the standard reduction potentials between the electroactive ions (cannot be modified).

In terms of hosts that can simultaneously intercalate two cations, at similar voltages, we identify maricite-$FePO_4$ (mp-776288, **Figure S12g** [143, 144]) to be useful in the simultaneous removal of Na (at 0.36 V vs. SHE) and Li (at 0.28 V vs. SHE), where only the Na-intercalated state is experimentally reported. Similarly, the high-pressure $\beta'$-$FePO_4$ phase (mp-25303, **Figure S12e** [145]) can intercalate Li (at 0.36 V vs. SHE) and Na (at 0.30 V vs. SHE), with the Li-intercalated phase being experimentally reported. The monoclinic-$FePO_4$ polymorph (mp-752872, $P2_1/c$, **Figure S12f**) that has $FeO_5$ bipyramidal units instead of the $FeO_6$ octahedra seen in the olivine, can theoretically intercalate both Ca and Mg at 0.28 and 0.30 V vs. SHE, respectively. $Fe_2(MoO_4)_3$ (mp-1042928, **Figure S12c**) is the final two ion intercalating host that we find with similar intercalation voltages of -0.057 and -0.141 V vs. SHE for Mg and Ca, respectively, with all structures being theoretical in this system.

We do not find any seawater metastable electrodes that intercalate more than two different ions at a similar voltage. However, three hosts that show the ability to intercalate three ions, namely, $Fe(PO_3)_3$ (mp-25310, **Figure S12i**), $NaCoPCO_7$ (mp-1101670, **Figure S12l**), and $LiFePCO_7$ (mp-1176697, **Figure S12k**), do exhibit similar voltages for the intercalation of two out of the three ions. For example, $Fe(PO_3)_3$ has an experimentally reported Li-intercalated structure, $LiFe(PO_3)_3$ (mp-504179 [146]) with an intercalation voltage of 0.64 V vs. SHE, which is close to its theoretical Na intercalation voltage of 0.56 V vs. SHE, but significantly different from the theoretical Mg intercalation voltage of 0.01 V vs. SHE. Similarly, the

$CoPCO_7$ host intercalates Li and Na at ∼1.1 V vs. SHE, while K intercalation occurs at a different voltage of 0.81 V vs. SHE. $Na_3CoPCO_7$ (mp-770948 [147]) is the only experimentally reported electrode in the $CoPCO_7$ host. Among all the intercalation reactions into $CoPCO_7$, only the sodiation of $Na_2CoPCO_7$ (mp-770988) yields coexisting phases that cover more than 80% of the seawater metastability window. The analogous Li (de)intercalation falls just short at 79% (**Figure S9d1**†), whereas the K reaction covers only 54% (**Figure S9d3**‡), as indicated by the hatched and faded points, respectively, in **Figure 6b**.

The $FePCO_7$ host can intercalate Li, Na, and K, where $LiFePCO_7$ (mp-1176697), $NaFePCO_7$ (mp-769633) and $KFePCO_7$ (mp-769579) constitute the most deintercalated phases. Sodiation of the theoretical $Na_2FePCO_7$ (mp-1176399) phase forms the experimentally reported topotactic structure $Na_3FePCO_7$ (mp-22135, [147]) at −0.14 V vs. SHE, which is close to the intercalation voltage of -0.2 V vs. SHE of the theoretical phase $K_3FePCO_7$ (mp-1575580). Other possible intercalation voltages with the $FePCO_7$ host, where the co-existing phase occupy 70 to 80% of the seawater metastability area are at 0.73 V vs. SHE, when $Na_3FePCO_7$ forms directly from the sodiation of $NaFePCO_7$, and at 1.04 V vs SHE when theoretical $K_2FePCO_7$ (mp-773453) forms upon K-intercalation of $KFePCO_7$. Interestingly, the presence of topotactic $LiFePCO_7$ (mp-1176697) and $Li_3FePCO_7$ (mp-25445) electrodes classifies $FePCO_7$ as a three-ion intercalating electrode, however both the Li-containing structures are not metastable under seawater operating conditions.

# 4 Discussion

Here, we used a high-throughput screening workflow (**Figure 1**) based on DFT-calculations, the conceptualization and construction of seawater Pourbaix diagrams, and the usage of modified metastability criteria and calculated intercalation voltages to identify electrode materials for electrochemical ion recovery (ion-selective hosts) and desalination (non-selective hosts) applications. Specifically, we screened through a set of 20,414 structures (**Figure 2**) containing Li, Mg, Ca, Na, or K from the MP project, evaluated their metastability and their ability to (de)intercalate under seawater conditions, and compared the structures containing different electroactive ions via computational graphs to identify 11 hosts that are ion-selective, 7 hosts that can intercalate two ions simultaneously, and the olivine-$FePO_4$ that can intercalate Li, Na, Mg, and K (**Figure 6**). Importantly, eight ion-selective and six non-selective (including olivine-$LiFePO_4$) electrode candidates that we identified as most promising exhibit at least one experimentally known composition/structure, highlighting their potential in experimental trials. A summary of the most promising candidates is compiled in **Table 1**.

One of the approximations involved in our work is in the way we construct our seawater Pourbaix diagrams. Typically, Pourbaix diagrams obtain the thermodynamically stable phase(s) by minimizing the Pourbaix potential, which is open to H and O (i.e., the system is in equilibrium with an infinite reservoir of H and O atoms) at different pH and applied potential. Thus, the classical Pourbaix potential is strictly meant for modeling the stability of a given solid (such as a potential electrode material considered here) in pure water or dilute solutions (e.g., **Figure 2c**) and not a seawater medium that contains 'large' reservoirs of non-H,O species, such as Cl, Na, Mg, S, etc. Indeed, including large reservoirs of non-H,O species within the Pourbaix potential requires the introduction of a chemical potential ($\mu$) for each species, which is non-trivial. For instance, $\mu_H$ and $\mu_O$ are tied to a constant $\mu_{H_2O}$ across pH and potentials [86, 87], allowing $\mu_H$ to be directly linked to pH (see **Section S2**). But the same approximation cannot be made for $\mu_{Cl}$, since Cl can form $Cl^-$, $ClO_4^-$, $HClO_{4(s)}$, or $ClO_{2(s)}$ depending on pH and potential, meaning $\mu_{Cl}$ (or $\mu_{HCl}$) cannot be assumed to be a constant across pH/potential like $\mu_{H_2O}$. However, we are interested in finding intercalation

electrodes that are stable in seawater and can capture cations, signifying that we cannot use the classical Pourbaix diagram *as is* implemented in `pymatgen`.

To circumvent the challenge of describing $\mu$ for additional species in our Pourbaix potential, we introduced the following modifications: (*i*) included all non-H,O elements in the aqueous reservoir (such as Cl) as part of the 'solid' also so that we can minimize the 'standard' Pourbaix potential, (*ii*) restricted our analysis to the top four most abundant elements found in seawater to reduce computational complexity (**Section S3**), (*iii*) calculated the decomposition energy of a phase by enumerating all combinations of reactants (where possible reactants vary as a function of pH and potential) that can react with a metastable electrode (**Section S5**), and (*iv*) characterize the reaction that yields the highest decomposition energy as the actual decomposition energy of a metastable electrode and evaluate against our 0.3 eV atom$^{-1}$ threshold (**Sections 2.4**, **S6**, and **Figure 3**). Note that modification (*i*) listed above actually restricts our stability evaluation to a smaller chemical space since the ratios of all non-H,O elements are fixed in the combined solid+solution system to satisfy mass conservation. This limitation is partly compensated by modification (*iii*), where the enumeration of decomposition reactions allows for varying ratios of the species that are supposed to be already present in seawater to react with the metastable solid (electrode), and the tighter threshold used in modification (*iv*). However, we do acknowledge the imperfections of constructing seawater Pourbaix diagrams as done here and we will be developing a more rigorous thermodynamic formalism as part of follow-up work.

Besides the modifications to the Pourbaix potential, we assume an electrode to be ion-selective if MP does not contain any structure with another electroactive ion intercalated in the same host. As a consequence, the lack of data in MP could yield false positives, where an electrode seems to be ion-selective due to the absence of data rather than its intrinsic behavior. However, we expect the proposed experimentally known ion-selective electrodes (**Figure 6a** and **Table 1**) to be more reliable than the theoretical electrodes (yellow sets of **Figure 4**), as experimentally known electrodes are more likely to have been explored with alternate electroactive ions, where the lack of reported structures with other ions possibly indicates the tendency of the host to be ion-selective. Note that the set of hosts that can theoretically intercalate multiple ions but do not exhibit the required metastability (i.e., systems with faded symbols in **Figure 6b**), such as $Fe_2(SiO_3)_2$ (mp-1253019, mp-25240) and $Fe_2(PO_4)_3$ (mp-26582), can be considered as potentially ion-selective candidates as well.

Among the initial set of shortlisted candidates in panels a and b of **Figure 6**, we observe the recurrence of O, Fe, and P across several hosts. While the presence of O can be attributed to its abundance in the aqueous reservoir, the frequent occurrence of Fe and P can provide crucial insights into the chemistry of seawater (meta)stable electrodes. For instance, **Figure S15b** shows that the final set of shortlisted candidates (including theoretical hosts) has a significantly greater fraction of structures that contain Fe (74.2%) and P (72%), as compared to their fractions in the full dataset in (32.9% Fe and 33.4% P, **Figure S15a**). A phenomenological explanation for the occurrence of P and Fe can be attempted based on their individual seawater Pourbaix diagrams, as shown in **Figure S14a,b**. Dark-green (light-green) regions in **Figure S14** contain at least one solid phase (only aqueous species). In the seawater Pourbaix diagram of Fe (**Figure S14a**) we mostly observe dark-green regions that can be attributed to stable $Fe_2O_3$ (explaining the occurrence of Fe-containing candidates), while light-green regions appear only at lower potentials where Fe dissolves into $FeOH^+$. On the other hand, most of the seawater stability window is light-green for P, indicating presence of only aqueous species (**Figure S14b**), which does not explain our observation of the occurrence of P among candidate seawater metastable electrodes. This indicates that the occurrence of P can not be explained by considering single element Pourbaix diagrams alone.

Table 1: Summary of the most promising ion-selective and non-selective intercalation electrodes identified in this work.

| Host | Ion | Deintercalated formula | Deintercalated MP ID | Intercalated formula | Intercalated MP ID | Voltage (V vs. SHE) | Intersecting metastability area (%) |
|---|---|---|---|---|---|---|---|
| | | | *Ion-selective hosts* | | | | |
| $Fe_2(MoO_4)_3$ | Li | $Fe_2(MoO_4)_3$* | mp-21925 | $Li_2Fe_2(MoO_4)_3$* | mp-21778 | 0.08 | 91.6 |
| $Fe_2(PO_4)_3$ | Li | $Li_3Fe_2(PO_4)_3$* | mp-25993 | $Li_5Fe_2(PO_4)_3$ | mp-1177302 | −0.30 | 88.0 |
| $LiFeP_2O_7$ | Li | $LiFeP_2O_7$* | mp-19294 | $Li_2FeP_2O_7$ | mp-779056 | 0.02 | 88.0 |
| $NbCoO_4$ | Mg | $NbCoO_4$* | mp-31518 | $MgNb_2(CoO_4)_2$ | mp-2219413 | −0.12 | 87.3 |
| $Ti(FeO_2)_4$ | Mg | $Ti(FeO_2)_4$ | mp-35482 | $MgTi(FeO_2)_4$ | mp-2228463 | 0.53 | 85.1 |
| $TiFe_2O_5$ | Mg | $TiFe_2O_5$* | mp-19255 | $MgTi_2(Fe_2O_5)_2$ | mp-2229085 | −0.63 | 99.5 |
| $Ca_3Co_2(Si_2O_7)_2$ | Ca | $Ca_3Co_2(Si_2O_7)_2$ | mp-1256217 | $Ca_2CoSi_2O_7$* | mp-18786 | 0.76 | 87.3 |
| $CaFeMoO_6$ | Ca | $Ca_3Fe_2(MoO_6)_2$ | mp-1323783 | $Ca_2FeMoO_6$* | mp-18783 | −0.17 | 91.6 |
| $Na_2FeSiCO_7$ | Na | $Na_2FeSiCO_7$ | mp-772135 | $Na_3FeSiCO_7$ | mp-771204 | 1.16 | 80.1 |
| $NaFe_3(PO_4)_3$ | Na | $NaFe_3(PO_4)_3$* | mp-556692 | $Na_2Fe_3(PO_4)_3$* | mp-558822 | 1.04 | 88.0 |
| $TiO_2$ | K | $TiO_2$ | mp-1400963 | $KTi_{16}O_{32}$ | mp-757418 | −0.25 | 99.5 |
| | K | $KTi_{16}O_{32}$ | mp-757418 | $KTi_6O_{12}$ | mp-765472 | −0.53 | 99.5 |
| | | | *Non-selective hosts* | | | | |
| $FePO_4$ | Na | $FePO_4$ | mp-776288 | $NaFePO_4$* | mp-19226 | 0.36 | 88.0 |
| | Li | $FePO_4$ | mp-776288 | $LiFePO_4$ | mp-831160 | 0.28 | 83.3 |
| $FePO_4$ | Li | $FePO_4$* | mp-25303 | $LiFePO_4$* | mp-18951 | 0.36 | 88.0 |
| | Na | $FePO_4$* | mp-25303 | $NaFePO_4$ | mp-753672 | 0.30 | 88.0 |
| $FePO_4$ | Mg | $FePO_4$ | mp-752872 | $MgFe_4(PO_4)_4$ | mp-1234799 | 0.30 | 88.0 |
| | Ca | $FePO_4$ | mp-752872 | $CaFe_4(PO_4)_4$ | mp-1233687 | 0.28 | 88.0 |
| $Fe_2(MoO_4)_3$ | Ca | $Fe_2(MoO_4)_3$ | mp-1042928 | $Ca_3Fe_4(MoO_4)_6$ | mp-1043101 | −0.06 | 81.2 |
| | Mg | $Fe_2(MoO_4)_3$ | mp-1042928 | $Mg_3Fe_4(MoO_4)_6$ | mp-1042940 | −0.14 | 83.3 |
| $Fe(PO_3)_3$ | Li | $Fe(PO_3)_3$ | mp-25310 | $LiFe(PO_3)_3$* | mp-504179 | 0.65 | 80.8 |
| | Na | $Fe(PO_3)_3$ | mp-25310 | $NaFe(PO_3)_3$ | mp-764111 | 0.56 | 87.3 |
| | Mg | $Fe(PO_3)_3$ | mp-25310 | $MgFe_4(PO_3)_{12}$ | mp-2234300 | −0.01 | 84.4 |
| $FePCO_7$ | K | $KFePCO_7$ | mp-769579 | $K_2FePCO_7$ | mp-773453 | 1.04 | 79.4 |
| | Na | $NaFePCO_7$ | mp-769633 | $Na_3FePCO_7$* | mp-22135 | 0.73 | 79.4 |
| | Na | $Na_2FePCO_7$ | mp-1176399 | $Na_3FePCO_7$* | mp-22135 | −0.14 | 88.0 |
| | K | $K_2FePCO_7$ | mp-773453 | $K_3FePCO_7$ | mp-1575580 | −0.20 | 87.3 |
| $CoPCO_7$ | Na | $Na_2CoPCO_7$ | mp-770988 | $Na_3CoPCO_7$* | mp-770948 | 1.12 | 83.0 |
| | Li | $Li_2CoPCO_7$ | mp-25454 | $Li_3CoPCO_7$ | mp-25458 | 1.06 | 79.0 |
| | K | $KCoPCO_7$ | mp-773502 | $K_3CoPCO_7$ | mp-1580470 | 0.81 | 54.2 |
| $FePO_4$ (olivine) | Li | $FePO_4$* | mp-20361 | $LiFePO_4$* | mp-19017 | 0.46 | 88.0 |
| | Na | $FePO_4$* | mp-20361 | $Na_2Fe_3(PO_4)_3$* | mp-1195335 | 0.34 | 88.0 |
| | Na | $Na_2Fe_3(PO_4)_3$* | mp-1195335 | $NaFePO_4$* | mp-746030 | 0.21 | 88.0 |
| | Mg | $FePO_4$* | mp-20361 | $MgFe_4(PO_4)_4$ | mp-2234827 | −0.17 | 88.0 |
| | K | $FePO_4$* | mp-20361 | $KFePO_4$ | mp-746071 | −0.25 | 70.4 |

Phases with an asterisk (*) denote experimental structures. $Ti(FeO_2)_4$ for Mg intercalation, $Na_2FeSiCO_7$ for Na intercalation, and $TiO_2$ for K intercalation are the pure theoretical ion-selective hosts listed here. Similarly, $Fe_2(MoO_4)_3$ and $FePO_4$ (mp-725872), both for Mg-Ca intercalation, are the pure theoretical non-selective hosts. All voltages are in V vs. SHE.

An examination of the combined Fe-P seawater Pourbaix diagram (**Figure S14c**) offers a better explanation on the frequent occurrence of Fe and P among candidate electrodes compared to the individual Fe and P Pourbaix diagrams. For example, the light-green regions of similar voltages ($-0.5$ to $-0.2$V) and pH (7 to 8.4), where Fe and P individually dissolve to form $FeOH^+$ and $HPO_4^{2-}$, the combined Fe-P system forms a dark-green region with a stable $Fe_3(PO_4)_2$ solid. Thus, while P by itself dissolves, the presence of Fe leads P to form a stable solid phase. Hence, the combined presence of Fe and P widens the (meta)stability of any electrode phase that forms $Fe_3(PO_4)_2$ as a decomposition product, which is not possible with the sole presence of either Fe or P in the electrode, explaining the frequency of occurrence of both Fe and P in several candidate electrodes. Further, we observe P and Si to be the most commonly ocurring element in candidate electrodes when considering the presence of a transition metal (see **Figure ??**), highlighting the solid-stabilizing effect of P in multi-component seawater systems.

While our workflow identifies olivine-$FePO_4$ as a promising desalination electrode (**Figure 6**), we do not identify the experimentally explored spinel-$Mn_2O_4$ as a candidate host for electrochemical ion capture, which can largely be attributed to the tendency of Mn to dissolve in aqueous media [5, 55, 56, 148]. For example, we do find that Li intercalation in $MnO_2$ is feasible in seawater conditions (**Figure S5b**), but the area of metastability of the $MnO_2$ host is only 25% of the seawater stability window, thus making it susceptible to overpotentials. The tendency of $MnO_2$ to dissolve is primarily due to the formation of stable $MnO_4^-$ species at higher potentials and $Mn^{2+}$ at lower potentials, within the seawater stability window. Also, the presence of P with Mn (**Figure S14d**), unlike the case with Fe, does not cause any stabilizing effect via the formation of a stable and solid Mn-based phosphate. Thus, Mn dissolution driving a reduction in the metastability area is the primary reason that Mn-containing hosts are not shortlisted in our screening.

Other approximations in our workflow include considering only aqueous species (i.e., ions and complexes) that contain a single non-H,O element, as constrained by the availability of experimental aqueous species data in MP [86], which excludes complexes such as $NaSO_4^-$. Additionally, all solid energies used in our work are DFT-calculated, using periodic boundary conditions, signifying that configurationally disordered, amorphous, and defective solids have not been considered. Further, errors associated with DFT calculations, such as deficiencies in the description of electronic exchange and correlation in solids, affect our predictions as well. Also, we approximate the activities of the aqueous species by their corresponding molar concentrations to obtain the Pourbaix potential of the dissolved species. Thus, a non-H,O element dissolving from a solid has to be equilibrated with respect to a constant pre-determined concentration in solution, which are the respective seawater concentrations for Cl, Na, Mg, S, Ca, and K and the dilute limit of $10^{-6}$ M for all other elements.

Also, we do not explore the thermodynamic and/or kinetic effects of co-intercalation of multiple ions, majorly due to the lack of available co-intercalated structures. Thus, we only report whether co-intercalation is possible within an electrode under seawater conditions (**Figure 6b**). We do observe a high number of Li-based candidates in our screening (**Figure 2b**), which can largely be attributed to the bias in our dataset that itself derives from the extensive research done on LIBs. Indeed, the number of queried phases are in the sequence Li>Mg>Na>Ca>K, while the shortlisted candidates follow the order Li>Mg>Ca>Na>K (**Figure 4**). In any case, we expect all our predicted non-Li intercalating structures to not intercalate any Li at all, given that it is more likely for prior studies to attempt Li intercalation than other ionic intercalation in any host. Furthermore, we do not evaluate kinetic properties of hosts, such as the activation barrier for ionic migration of the electroactive ion(s), which can play a role in the practical feasibility of using an electrode for ion capture.

# 5 Conclusion

In summary, we have used a high-throughput DFT-based screening approach to identify novel intercalation electrodes for electrochemical ion recovery and desalination, which are crucial technologies that can aid in our transition to a sustainable energy future and better use of our available water sources. Upon querying 20,414 structures containing Li, Mg, Ca, Na, or K along with redox-active TM(s) and anion(s) from the MP, we developed a four-step screening workflow involving *i*) the construction of seawater Pourbaix diagrams to include the effects of ions normally present in seawater, *ii*) the calculation of the decomposition energy of metastable electrodes systematically using the corresponding seawater Pourbaix diagrams, *iii*) the determination of the metastability of (de)intercalated structures based on a modified (<0.3 eV atom$^{-1}$) threshold, *iv*) the evaluation of average intercalation voltages and intersecting metastability area for deintercalated-intercalated pairs of structures (to be >80% of the seawater stability window), and *v*) the identification of promising ion-selective and non-selective candidates via the construction of computational graphs to encode selectivity across hosts. Importantly, we identified eight experimentally known hosts and three theoretical hosts to be promising ion-selective candidates, four experimentally known hosts that can intercalate two ions simultaneously, and olivine-$FePO_4$ as the closest candidate to an ideal desalination electrode. Some of the promising materials identified in our workflow, which have not been explored yet for selective ion recovery from aqueous media, include, $Fe_2(MoO_4)_3$, $Li_3Fe_2(PO_4)_3$, $LiFeP_2O_7$ for Li, $NbCoO_4$ and $TiFe_2O_5$ for Mg, $Ca_3Co_2(Si_2O_7)_2$ and $Ca_3Fe_2(MoO_6)_2$ for Ca, $Fe_7(PO_4)_6$ and $NaFe_3(PO_4)_3$ for Na, and hollandite-$TiO_2$ for K. We are hopeful that our high-throughput screening framework, qualitative trends and thermodynamic insights, and the final list of identified candidates accelerates the practical development of electrochemical ion capture technologies.

# Acknowledgments

G.S.G. acknowledges funding by the Science and Engineering Research Board, Government of India, under the sanction number IPA/2021/000007. S.P. thanks the Ministry of Human Resource Development, Government of India, for financial assistance. A.K., M.H., and H.G.S. acknowledge funding by the German Federal Ministry of Research, Technology and Space (BMFTR) and the Ministry of Economic Affairs, Industry, Climate Action and Energy of the State of North Rhine-Westphalia through the project HC-H2. M.H. and H.G.S. acknowledge funding from the German Federal Ministry of Research, Technology and Space (BMFTR) via project 05K24CJ1. A.K. thanks the Stiftung Stipendien-Fonds of the German Chemical Industry Association (Verband der Chemischen Industrie, VCI) for a Kekulé fellowship. S.P. and G.S.G. acknowledge the computational resources provided by the Supercomputer Education and Research Centre, IISc, for enabling some of the calculations showcased in this work. The authors gratefully acknowledge the computing time provided to them on the high-performance computers noctua1 and noctua2 at the NHR Center PC2. This was funded by the Federal Ministry of Education and Research and the state governments participating on the basis of the resolutions of the GWK for national high-performance computing at universities (www.nhrverein.de/unsere-partner). The computations for this research project were performed using computing resources under projects hpc-prf-emdft and hpc-prf-desal. The authors also gratefully acknowledge the Jülich Supercomputing Centre at Forschungszentrum Jülich, Germany, for access to the JURECA supercomputer under the project 'desal', which enabled some of the calculations reported in this work.

## Data and code availability

All calculated data and the scripts used in this work are available freely online on our GitHub repository.

## Conflicts of interest

The authors have no conflicts of interest to declare.

## References


[1] Sujay S Kaushal, Gene E Likens, Paul M Mayer, Ruth R Shatkay, Sydney A Shelton, Stanley B Grant, Ryan M Utz, Alexis M Yaculak, Carly M Maas, Jenna E Reimer, et al. The anthropogenic salt cycle. *Nature Reviews Earth & Environment*, 4(11):770–784, 2023.

[2] Noman Khalid Khanzada, Raed A Al-Juboori, Yazan Ibrahim, Muzamil Khatri, Farah Ejaz Ahmed, Alicia Kyoungjin An, and Nidal Hilal. Desalination and the middle east: research, practices, implications, and prospects. *npj Clean Water*, 2026.

[3] Margaret G O'Connell, Neha Rajendran, Menachem Elimelech, Jack Gilron, and Jennifer B Dunn. Analysis of energy, water, land and cost implications of zero and minimal liquid discharge desalination technologies. *Nature Water*, 2(11):1116–1127, 2024.

[4] JG Gamaethiralalage, K Singh, S Sahin, J Yoon, M Elimelech, ME Suss, P Liang, PM Biesheuvel, R Linzmeyer Zornitta, and LCPM De Smet. Recent advances in ion selectivity with capacitive deionization. *Energy & Environmental Science*, 14(3):1095–1120, 2021.

[5] Pattarachai Srimuk, Xiao Su, Jeyong Yoon, Doron Aurbach, and Volker Presser. Charge-transfer materials for electrochemical water desalination, ion separation and the recovery of elements. *Nature Reviews Materials*, 5(7):517–538, 2020.

[6] Zhenghao Meng, Han Sun, Ichiro Daigo, Yuru Guan, and Yuli Shan. Technological risks disrupting trade stability in the global lithium supply chain network. *IScience*, 28(7), 2025.

[7] EA Olivetti, G Ceder, Ge G Gaustad, and X Fu. Lithium-ion battery supply chain considerations: analysis of potential bottlenecks in critical metals. joule 1: 229–243, 2017.

[8] Alberto Battistel, Maria Sofia Palagonia, Doriano Brogioli, Fabio La Mantia, and Rafael Trócoli. Electrochemical methods for lithium recovery: a comprehensive and critical review. *Advanced Materials*, 32(23):1905440, 2020.

[9] Mineral Commodity Summaries. Lithium (usgs, 2021), 2025.

[10] María L Vera, Walter R Torres, Claudia I Galli, Alexandre Chagnes, and Victoria Flexer. Environmental impact of direct lithium extraction from brines. *Nature Reviews Earth & Environment*, 4(3):149–165, 2023.

[11] Mauro Pasta, Alberto Battistel, and Fabio La Mantia. Batteries for lithium recovery from brines. *Energy & Environmental Science*, 5(11):9487–9491, 2012.

[12] Longqian Xu, Bing Zhao, Xudong Zhang, Weifan Liu, Daniel Rau, Deli Wu, Wencai Zhang, Chong Liu, Zhong Liu, and Shihong Lin. Membrane and electrochemical separations for direct lithium extraction. *Nature Chemical Engineering*, 2(9):551–567, 2025.

[13] Lingchen Kong, Gangbin Yan, Kejia Hu, Yongchang Yu, Nicole Conte, Kevin R Mckenzie Jr, Michael J Wagner, Stephen G Boyes, Hanning Chen, Chong Liu, et al. Electro-driven direct lithium extraction from geothermal brines to generate battery-grade lithium hydroxide. *Nature Communications*, 16(1):806, 2025.

[14] William T Stringfellow and Patrick F Dobson. Technology for the recovery of lithium from geothermal brines. *Energies*, 14(20):6805, 2021.

[15] Ugo Bardi. Extracting minerals from seawater: an energy analysis. *Sustainability*, 2(4):980–992, 2010.

[16] Chong Liu, Yanbin Li, Dingchang Lin, Po-Chun Hsu, Bofei Liu, Gangbin Yan, Tong Wu, Yi Cui, and Steven Chu. Lithium extraction from seawater through pulsed electrochemical intercalation. *Joule*, 4(7):1459–1469, 2020.

[17] Zhen Li, Chunyang Li, Xiaowei Liu, Li Cao, Peipei Li, Ruicong Wei, Xiang Li, Dong Guo, Kuo-Wei Huang, and Zhiping Lai. Continuous electrical pumping membrane process for seawater lithium mining. *Energy & Environmental Science*, 14(5):3152–3159, 2021.

[18] Seoni Kim, Jiye Kim, Seonghwan Kim, Jaehan Lee, and Jeyong Yoon. Electrochemical lithium recovery and organic pollutant removal from industrial wastewater of a battery recycling plant. *Environmental Science: Water Research & Technology*, 4(2):175–182, 2018.

[19] Ersha Fan, Li Li, Zhenpo Wang, Jiao Lin, Yongxin Huang, Ying Yao, Renjie Chen, and Feng Wu. Sustainable recycling technology for li-ion batteries and beyond: challenges and future prospects. *Chemical reviews*, 120(14):7020–7063, 2020.

[20] Amit Kumar, Hiroki Fukuda, T Alan Hatton, and John H Lienhard. Lithium recovery from oil and gas produced water: a need for a growing energy industry. *ACS Energy Letters*, 4(6):1471–1474, 2019.

[21] Zhen Li, I-Chun Chen, Li Cao, Xiaowei Liu, Kuo-Wei Huang, and Zhiping Lai. Lithium extraction from brine through a decoupled and membrane-free electrochemical cell design. *Science*, 385(6716):1438–1444, 2024.

[22] Gangbin Yan, Mingzhan Wang, Grant T Hill, Siqi Zou, and Chong Liu. Defining the challenges of li extraction with olivine host: the roles of competitor and spectator ions. *Proceedings of the National Academy of Sciences*, 119(31):e2200751119, 2022.

[23] Quan Peng, Ruoyu Wang, Zilin Zhao, Shihong Lin, Ying Liu, Dianyu Dong, Zheng Wang, Yiman He, Yuzhang Zhu, Jian Jin, et al. Extreme li-mg selectivity via precise ion size differentiation of polyamide membrane. *Nature Communications*, 15(1):2505, 2024.

[24] European Parliament and Council of the European Union. Directive (EU) 2020/2184 of the European Parliament and of the Council of 16 December 2020 on the quality of water intended for human consumption (recast). Official Journal of the European Union, L 435, 23.12.2020, pp. 1–62, 2020. CELEX: 32020L2184.

[25] Uttam K. Saha, Stephanie Butcher, Gary L. Hawkins, Wesley Porter, and Jason Lessl. Irrigation water quality for agriculture. Bulletin 1448, University of Georgia Cooperative Extension, Athens, GA, June 2026.

[26] Lei Wang, Kathleen Frisella, Pattarachai Srimuk, Oliver Janka, Guido Kickelbick, and Volker Presser. Electrochemical lithium recovery with lithium iron phosphate: what causes performance degradation and how can we improve the stability? *Sustainable Energy & Fuels*, 5(12):3124–3133, 2021.

[27] Yanjie Zheng, Rodrigo A Caceres Gonzalez, Kelsey B Hatzell, and Marta C Hatzell. Large-scale solar-thermal desalination. *Joule*, 5(8):1971–1986, 2021.

[28] Menachem Elimelech and William A Phillip. The future of seawater desalination: energy, technology, and the environment. *science*, 333(6043):712–717, 2011.

[29] Alexander V Dudchenko, Timothy V Bartholomew, and Meagan S Mauter. High-impact innovations for high-salinity membrane desalination. *Proceedings of the National Academy of Sciences*, 118(37):e2022196118, 2021.

[30] Weifan Liu, Joshua L Livingston, Li Wang, Zhangxin Wang, Martina Del Cerro, Saad A Younssi, Razi Epsztein, Menachem Elimelech, and Shihong Lin. Pressure-driven membrane desalination. *Nature Reviews Methods Primers*, 4(1):10, 2024.

[31] Sultan Alnajdi, Ali Naderi Beni, Albraa A Alsaati, Mitul Luhar, Amy E Childress, and David M Warsinger. Practical minimum energy use of seawater reverse osmosis. *Joule*, 8(11):3088–3105, 2024.

[32] Edward Jones, Manzoor Qadir, Michelle TH Van Vliet, Vladimir Smakhtin, and Seong-mu Kang. The state of desalination and brine production: A global outlook. *Science of the total environment*, 657:1343–1356, 2019.

[33] Valerie A Niemann, Marten Huck, Hans-Georg Steinrück, Michael F Toney, William A Tarpeh, and Sharon E Bone. X-ray absorption spectroscopy reveals mechanisms of calcium and silicon fouling on reverse osmosis membranes used in wastewater reclamation. *ACS ES&T Water*, 3(8):2627–2637, 2023.

[34] Sharon E Bone, Hans-Georg Steinrück, and Michael F Toney. Advanced characterization in clean water technologies. *Joule*, 4(8):1637–1659, 2020.

[35] Anurag Bajpayee, Tengfei Luo, Andrew Muto, and Gang Chen. Very low temperature membrane-free desalination by directional solvent extraction. *Energy & Environmental Science*, 4(5):1672–1675, 2011.

[36] Jiaji Guo, Zachary D Tucker, Yu Wang, Brandon L Ashfeld, and Tengfei Luo. Ionic liquid enables highly efficient low temperature desalination by directional solvent extraction. *Nature Communications*, 12(1):437, 2021.

[37] Elizabeth Dach, Juliana Marston, Sara Abu-Obaid, Allison Peng, and Ngai Yin Yip. A novel approach for direct lithium extraction from alkali metal cations in brine mixtures using thermally switchable solvents. *Joule*, 10(2), 2026.

[38] Yi Ding, David Harvey, and Nien-Hwa Linda Wang. Two-zone ligand-assisted displacement chromatography for producing high-purity praseodymium, neodymium, and dysprosium with high yield and high productivity from crude mixtures derived from waste magnets. *Green Chemistry*, 22(12):3769–3783, 2020.

[39] Ziye Dong, Joseph A Mattocks, Gauthier J-P Deblonde, Dehong Hu, Yongqin Jiao, Joseph A Cotruvo Jr, and Dan M Park. Bridging hydrometallurgy and biochemistry: a protein-based process for recovery and separation of rare earth elements. *ACS Central Science*, 7(11):1798–1808, 2021.

[40] Joseph A Mattocks, Jonathan J Jung, Chi-Yun Lin, Ziye Dong, Neela H Yennawar, Emily R Featherston, Christina S Kang-Yun, Timothy A Hamilton, Dan M Park, Amie K Boal, et al. Enhanced rare-earth separation with a metal-sensitive lanmodulin dimer. *Nature*, 618(7963):87–93, 2023.

[41] Mauro Pasta, Colin D Wessells, Yi Cui, and Fabio La Mantia. A desalination battery. *Nano letters*, 12(2):839–843, 2012.

[42] Kyle N Knust, Dzmitry Hlushkou, Robbyn K Anand, Ulrich Tallarek, and Richard M Crooks. Electrochemically mediated seawater desalination. *Angewandte Chemie*, 125(31):8265–8268, 2013.

[43] Sung-il Jeon, Hong-ran Park, Jeong-gu Yeo, SeungCheol Yang, Churl Hee Cho, Moon Hee Han, and Dong Kook Kim. Desalination via a new membrane capacitive deionization process utilizing flow-electrodes. *Energy & Environmental Science*, 6(5):1471–1475, 2013.

[44] Matthew E Suss, Slawomir Porada, Xiaowei Sun, P Maarten Biesheuvel, Jeyong Yoon, and Volker Presser. Water desalination via capacitive deionization: what is it and what can we expect from it? *Energy & Environmental Science*, 8(8):2296–2319, 2015.

[45] Vu Q Do, Erik R Reale, Irwin C Loud IV, Paul G Rozzi, Haosen Tan, David A Willis, and Kyle C Smith. Embedded, micro-interdigitated flow fields in high areal-loading intercalation electrodes towards seawater desalination and beyond. *Energy & Environmental Science*, 16(7):3025–3039, 2023.

[46] Longqian Xu, Weifan Liu, Xudong Zhang, Wei Tang, Dong-Ju Lee, Zezhou Yang, Zheng Chen, and Shihong Lin. Pseudo-continuous and scalable electrochemical ion pumping with circuit-switching-induced ion shuttling. *Nature Water*, 2(10):999–1008, 2024.

[47] Yuecheng Xiong, Jingwen Zhou, Pengyi Lu, Jinwen Yin, Yunhao Wang, and Zhanxi Fan. Electrochemical lithium extraction from aqueous sources. *Matter*, 5(6):1760–1791, 2022.

[48] Matthew E Suss and Volker Presser. Water desalination with energy storage electrode materials. *Joule*, 2(1):10–15, 2018.

[49] Bruce Dunn, Haresh Kamath, and Jean-Marie Tarascon. Electrical energy storage for the grid: a battery of choices. *Science*, 334(6058):928–935, 2011.

[50] R Trócoli, A Battistel, and F La Mantia. Nickel hexacyanoferrate as suitable alternative to ag for electrochemical lithium recovery. *ChemSusChem*, 8(15):2514–2519, 2015.

[51] Rafael Trócoli, Collins Erinmwingbovo, and Fabio La Mantia. Optimized lithium recovery from brines by using an electrochemical ion-pumping process based on $\lambda$-mno2 and nickel hexacyanoferrate. *ChemElectroChem*, 4(1):143–149, 2017.

[52] Along Zhao, Jincheng Liu, Xinping Ai, Hanxi Yang, and Yuliang Cao. Highly selective and pollution-free electrochemical extraction of lithium by a polyaniline/lixmn2o4 cell. *ChemSusChem*, 12(7):1361–1367, 2019.

[53] Marten Huck, Andreas Kuhlmann, Jakub Drnec, Vinh Hoang, Shanling Ji, Emil Skrentny, Christian Sternemann, Steffen Tober, Valentin Vinci, and Hans-Georg Steinrück. Toward understanding li-ion intercalation in limn2o4 electrodes for direct lithium extraction. 2026.

[54] JinKiong Ling, Chelladurai Karuppiah, Syam G Krishnan, MV Reddy, Izan Izwan Misnon, Mohd Hasbi Ab Rahim, Chun-Chen Yang, and Rajan Jose. Phosphate polyanion materials as high-voltage lithium-ion battery cathode: a review. *Energy & Fuels*, 35(13):10428–10450, 2021.

[55] CY Ouyang, SQ Shi, and MS Lei. Jahn–teller distortion and electronic structure of limn2o4. *Journal of Alloys and Compounds*, 474(1-2):370–374, 2009.

[56] Yuxin Jiang, Liyuan Chai, Dehe Zhang, Fangping Ouyang, Xiangyuan Zhou, Sikpaam I Alhassan, Sailin Liu, Yingjie He, Lvji Yan, Haiying Wang, et al. Facet-controlled limn2o4/c as deionization electrode with enhanced stability and high desalination performance. *Nano-Micro Letters*, 14(1):176, 2022.

[57] Xiaohong Shang, Bin Hu, Pengfei Nie, Wei Shi, Taimoor Hussain, and Jianyun Liu. Lini0. 5mn1. 5o4-based hybrid capacitive deionization for highly selective adsorption of lithium from brine. *Separation and Purification Technology*, 258:118009, 2021.

[58] Anubhav Jain, Shyue Ping Ong, Geoffroy Hautier, Wei Chen, William Davidson Richards, Stephen Dacek, Shreyas Cholia, Dan Gunter, David Skinner, Gerbrand Ceder, et al. Commentary: The materials project: A materials genome approach to accelerating materials innovation. *APL materials*, 1(1), 2013.

[59] Pierre Hohenberg and Walter Kohn. Inhomogeneous electron gas. *Physical review*, 136(3B):B864, 1964.

[60] Walter Kohn and Lu Jeu Sham. Self-consistent equations including exchange and correlation effects. *Physical review*, 140(4A):A1133, 1965.

[61] Gerbrand Ceder, Y-M Chiang, DR Sadoway, MK Aydinol, Y-I Jang, and Biying Huang. Identification of cathode materials for lithium batteries guided by first-principles calculations. *Nature*, 392(6677):694–696, 1998.

[62] Geoffroy Hautier, Anubhav Jain, Shyue Ping Ong, Byoungwoo Kang, Charles Moore, Robert Doe, and Gerbrand Ceder. Phosphates as lithium-ion battery cathodes: an evaluation based on high-throughput ab initio calculations. *Chemistry of Materials*, 23(15):3495–3508, 2011.

[63] Debolina Deb and Gopalakrishnan Sai Gautam. Critical overview of polyanionic frameworks as positive electrodes for na-ion batteries. *Journal of Materials Research*, 37(19):3169–3196, 2022.

[64] Kang Xu. Electrolytes and interphases in li-ion batteries and beyond. *Chemical reviews*, 114(23):11503–11618, 2014.

[65] David S Hall, Ahmed Eldesoky, ER Logan, Erin Marie Tonita, Xiaowei Ma, and JR Dahn. Exploring classes of co-solvents for fast-charging lithium-ion cells. *Journal of The Electrochemical Society*, 165(10):A2365–A2373, 2018.

[66] Pekka Peljo and Hubert H Girault. Electrochemical potential window of battery electrolytes: the homo–lumo misconception. *Energy & Environmental Science*, 11(9):2306–2309, 2018.

[67] Yuki Yamada, Jianhui Wang, Seongjae Ko, Eriko Watanabe, and Atsuo Yamada. Advances and issues in developing salt-concentrated battery electrolytes. *Nature Energy*, 4(4):269–280, 2019.

[68] Liumin Suo, Oleg Borodin, Tao Gao, Marco Olguin, Janet Ho, Xiulin Fan, Chao Luo, Chunsheng Wang, and Kang Xu. "water-in-salt" electrolyte enables high-voltage aqueous lithium-ion chemistries. *Science*, 350(6263):938–943, 2015.

[69] Weibo Hua, Suning Wang, Michael Knapp, Steven J Leake, Anatoliy Senyshyn, Carsten Richter, Murat Yavuz, Joachim R Binder, Clare P Grey, Helmut Ehrenberg, et al. Structural insights into the formation and voltage degradation of lithium-and manganese-rich layered oxides. *Nature communications*, 10(1):5365, 2019.

[70] Yaozhi Liu, Lu Lin, Shuqi He, Hong Wu, Daihuo Liu, Dongliang Chao, and Xiaoqi Sun. Dual characteristics of mn2+ dissolution from manganese oxide cathode materials in aqueous zinc batteries: trade-offs between active material loss and double capacity contribution. *Energy & Environmental Science*, 19(11):3475–3486, 2026.

[71] Marcel Pourbaix. Atlas of electrochemical equilibria in aqueous solutions. *NACE*, 1966.

[72] Edward McCafferty and E McCafferty. Thermodynamics of corrosion: Pourbaix diagrams. *Introduction to corrosion science*, pages 95–117, 2010.

[73] Arunima K Singh, Joseph H Montoya, John M Gregoire, and Kristin A Persson. Robust and synthesizable photocatalysts for co2 reduction: a data-driven materials discovery. *Nature communications*, 10(1):443, 2019.

[74] Yizhan Zhang, Lin Wang, Elena Scivally, Kayla James, Evelyn McBride, Mahesh Dheerasinghe, Michael Shatruk, Yan Zeng, and Bin Ouyang. Aqueous stability of metallic materials and metal oxides. *Chemistry of Materials*, 2025.

[75] Xiaochen Du, Mengren Liu, Jiayu Peng, Hoje Chun, Alexander Hoffman, Bilge Yildiz, Lin Li, Martin Z Bazant, and Rafael Gómez-Bombarelli. Accelerating and enhancing thermodynamic simulations of electrochemical interfaces. *ACS Central Science*, 11(9):1558, 2025.

[76] Diego Garay-Ruiz and Marisol Martín-González. Enriching pourbaix diagrams for improved understanding of competitive electrochemical phases. *npj Computational Materials*, 2026.

[77] Ryan S Kingsbury, Andrew S Rosen, Ayush S Gupta, Jason M Munro, Shyue Ping Ong, Anubhav Jain, Shyam Dwaraknath, Matthew K Horton, and Kristin A Persson. A flexible and scalable scheme for mixing computed formation energies from different levels of theory. *npj Computational Materials*, 8(1):195, 2022.

[78] Naoaki Yabuuchi, Mitsue Takeuchi, Masanobu Nakayama, Hiromasa Shiiba, Masahiro Ogawa, Keisuke Nakayama, Toshiaki Ohta, Daisuke Endo, Tetsuya Ozaki, Tokuo Inamasu, et al. High-capacity electrode materials for rechargeable lithium batteries: Li3nbo4-based system with cation-disordered rock-salt structure. *Proceedings of the National Academy of Sciences*, 112(25):7650–7655, 2015.

[79] Chenchen Wang, Luojia Liu, Shuo Zhao, Yanchen Liu, Yubo Yang, Haijun Yu, Suwon Lee, Gi-Hyeok Lee, Yong-Mook Kang, Rong Liu, et al. Tuning local chemistry of p2 layered-oxide cathode for high energy and long cycles of sodium-ion battery. *Nature communications*, 12(1):2256, 2021.

[80] T Ichitsubo, S Yagi, R Nakamura, Y Ichikawa, S Okamoto, K Sugimura, T Kawaguchi, A Kitada, M Oishi, T Doi, et al. A new aspect of chevrel compounds as positive electrodes for magnesium batteries. *Journal of Materials Chemistry A*, 2(36):14858–14866, 2014.

[81] Mariyappan Sathiya, Gwenaëlle Rousse, K Ramesha, CP Laisa, Hervé Vezin, Moulay Tahar Sougrati, Marie-Liesse Doublet, Dominique Foix, Danielle Gonbeau, W Walker, et al. Reversible anionic redox chemistry in high-capacity layered-oxide electrodes. *Nature materials*, 12(9):827–835, 2013.

[82] Yuqi Wu, Ke Zhou, Fucheng Ren, Yang Ha, Ziteng Liang, Xuefan Zheng, Zhenyu Wang, Wu Yang, Maojie Zhang, Mingzeng Luo, et al. Highly reversible li 2 ruo 3 cathodes in sulfide-based all solid-state lithium batteries. *Energy & Environmental Science*, 15(8):3470–3482, 2022.

[83] Paul E Pearce, Arnaud J Perez, Gwenaelle Rousse, Mathieu Saubanère, Dmitry Batuk, Dominique Foix, Eric McCalla, Artem M Abakumov, Gustaaf Van Tendeloo, Marie-Liesse Doublet, et al. Evidence for anionic redox activity in a tridimensional-ordered li-rich positive electrode $\beta$-li2iro3. *Nature materials*, 16(5):580–586, 2017.

[84] Nicholas H Bashian, Shiliang Zhou, Mateusz Zuba, Alex M Ganose, Joseph W Stiles, Allyson Ee, David S Ashby, David O Scanlon, Louis FJ Piper, Bruce Dunn, et al. Correlated polyhedral rotations in the absence of polarons during electrochemical insertion of lithium in reo3. *ACS Energy Letters*, 3(10):2513–2519, 2018.

[85] WT Thompson, MH Kaye, Christopher W Bale, and AD Pelton. Pourbaix diagrams for multielement systems. *Uhlig's corrosion handbook*, 3:103–109, 2011.

[86] Kristin A Persson, Bryn Waldwick, Predrag Lazic, and Gerbrand Ceder. Prediction of solid-aqueous equilibria: Scheme to combine first-principles calculations of solids with experimental aqueous states. *Physical Review B—Condensed Matter and Materials Physics*, 85(23):235438, 2012.

[87] Anjli M Patel, Jens K Nørskov, Kristin A Persson, and Joseph H Montoya. Efficient pourbaix diagrams of many-element compounds. *Physical Chemistry Chemical Physics*, 21(45):25323–25327, 2019.

[88] Wenhao Sun, Daniil A Kitchaev, Denis Kramer, and Gerbrand Ceder. Non-equilibrium crystallization pathways of manganese oxides in aqueous solution. *Nature communications*, 10(1):573, 2019.

[89] Arunima K Singh, Lan Zhou, Aniketa Shinde, Santosh K Suram, Joseph H Montoya, Donald Winston, John M Gregoire, and Kristin A Persson. Electrochemical stability of metastable materials. *Chemistry of Materials*, 29(23):10159–10167, 2017.

[90] Shyue Ping Ong, William Davidson Richards, Anubhav Jain, Geoffroy Hautier, Michael Kocher, Shreyas Cholia, Dan Gunter, Vincent L Chevrier, Kristin A Persson, and Gerbrand Ceder. Python materials genomics (pymatgen): A robust, open-source python library for materials analysis. *Computational Materials Science*, 68:314–319, 2013.

[91] James W Johnson, Eric H Oelkers, and Harold C Helgeson. Supcrt92: A software package for calculating the standard molal thermodynamic properties of minerals, gases, aqueous species, and reactions from 1 to 5000 bar and 0 to 1000 c. *Computers & Geosciences*, 18(7):899–947, 1992.

[92] Marcel Pourbaix. Atlas of electrochemical equilibria in aqueous solutions. *(No Title)*, 1974.

[93] Li-Qing Jiang, Brendan R Carter, Richard A Feely, Siv K Lauvset, and Are Olsen. Surface ocean ph and buffer capacity: past, present and future. *Scientific reports*, 9(1):18624, 2019.

[94] MK Aydinol, AF Kohan, Gerbrand Ceder, Kang Cho, and JJPRB Joannopoulos. Ab initio study of lithium intercalation in metal oxides and metal dichalcogenides. *Physical Review B*, 56(3):1354, 1997.

[95] Rahul Malik, Fei Zhou, and Gerbrand Ceder. Kinetics of non-equilibrium lithium incorporation in lifepo4. *Nature materials*, 10(8):587–590, 2011.

[96] Calin Wurm, Mathieu Morcrette, Gwenaelle Rousse, Loïc Dupont, and Christian Masquelier. Lithium insertion/extraction into/from limx2o7 compositions (m= fe, v; x= p, as) prepared via a solution method. *Chemistry of materials*, 14(6):2701–2710, 2002.

[97] AK Padhi, KS Nanjundaswamy, C Masquelier, S Okada, and JB Goodenough. Effect of structure on the fe3+/fe2+ redox couple in iron phosphates. *Journal of the Electrochemical Society*, 144(5):1609–1613, 1997.

[98] Sébastien Patoux, Călin Wurm, Mathieu Morcrette, Gwenaëlle Rousse, and Christian Masquelier. A comparative structural and electrochemical study of monoclinic li3fe2 (po4) 3 and li3v2 (po4) 3. *Journal of Power Sources*, 119:278–284, 2003.

[99] Ethan Paharik, Patrick Cantwell, and Gary Koenig. Iron phosphate polyanion compounds as anodes for aqueous lithium-ion batteries. *Electrochemical Society Transactions 232*, 80(10):171–182, 2017.

[100] A Manthiram and JB Goodenough. Lithium insertion into fe2 (mo4) 3 frameworks: comparison of m= w with m= mo. *Journal of Solid State Chemistry*, 71(2):349–360, 1987.

[101] U Lehmann and Hk Müller-Buschbaum. Einkristalle von conbo4 mit alnbo4-struktur. *Zeitschrift für anorganische und allgemeine Chemie*, 471(1):85–88, 1980.

[102] M Drofenik, L Golič, D Hanzel, V Kraševec, A Prodan, M Bakker, and D Kolar. A new monoclinic phase in the fe2o3 tio2 system. i. structure determination and mössbauer spectroscopy. *Journal of Solid State Chemistry*, 40(1):47–51, 1981.

[103] Weixin Xu, Donald R Peacor, Wayne A Dollase, Rob Van der Voo, and Rick Beaubouef. Transformation of titanomagnetite to titanomaghemite: A slow, two-step, oxidation-ordering process in morb. *American Mineralogist*, 82(11-12):1101–1110, 1997.

[104] Pieremanuele Canepa, Shou-Hang Bo, Gopalakrishnan Sai Gautam, Baris Key, William D Richards, Tan Shi, Yaosen Tian, Yan Wang, Juchuan Li, and Gerbrand Ceder. High magnesium mobility in ternary spinel chalcogenides. *Nature communications*, 8(1):1759, 2017.

[105] Gopalakrishnan Sai Gautam, Pieremanuele Canepa, Alexander Urban, Shou-Hang Bo, and Gerbrand Ceder. Influence of inversion on mg mobility and electrochemistry in spinels. *Chemistry of Materials*, 29(18):7918–7930, 2017.

[106] JA Alonso, MT Casais, MJ Martínez-Lope, JL Martínez, P Velasco, A Munoz, and MT Fernández-Díaz. Preparation, crystal structure, and magnetic and magnetotransport properties of the double perovskite ca2femoo6. *Chemistry of Materials*, 12(1):161–168, 2000.

[107] KENJI Hagiya, Masaaki Ohmasa, and Kazuaki Iishi. The modulated structure of synthetic co-åkermanite, ca2cosi2o7. *Structural Science*, 49(2):172–179, 1993.

[108] Matteo Ardit, Giuseppe Cruciani, and Michele Dondi. Local structural relaxation around co2+ along the hardystonite–co-åkermanite melilite solid solution. *Physics and Chemistry of Minerals*, 39(9):713–723, 2012.

[109] K Kusaka, K Hagiya, M Ohmasa, Y Okano, M Mukai, K Iishi, and N Haga. Determination of structures of ca2cosi2o7, ca2mgsi2o7, and ca2 (mg0. 55fe0. 45) si2o7 in incommensurate and normal phases and observation of diffuse streaks at high temperature. *Physics and Chemistry of Minerals*, 28(3):150–166, 2001.

[110] Arturo Torres, Jose Luis Casals, and M Elena Arroyo-de Dompablo. Enlisting potential cathode materials for rechargeable ca batteries. *Chemistry of Materials*, 33(7):2488–2497, 2021.

[111] M Kimata. Four-coordinated co2+ cation in ca2cosi2o7. *Naturwissenschaften*, 69(1):40–41, 1982.

[112] Li-Ying Duan, Fu-Chen Liu, En-Bo Wang, Yang-Guang Li, Chang-Wen Hu, and Lin Xu. Hydrothermal synthesis and properties of open-framework mixed-valence iron phosphates fe2lll fell1. 5 (po4) 3 with three-dimensional structure. *Chinese Journal of Chemistry*, 22(1):55–59, 2004.

[113] I Vencato, LD Moreira, E Mattievich, and YP Mascarenhas. The crystal-structure of synthetic fe42+ fe33+ (po3oh)(po4) 5. *JOURNAL OF THE BRAZILIAN CHEMICAL SOCIETY*, 5(1):43–51, 1994.

[114] Yu A Gorbunov, Boris Alekseevich Maksimov, Yurii Konstantinovich Kabalov, AN Ivashchenko, Oleg Konstantinovich Melnikov, and Nikolai Vasil'evich Belov. Crystal structure of fe_3^2+fe_4^3+po_4_6. In *Doklady Akademii Nauk*, volume 254, pages 873–877. Russian Academy of Sciences, 1980.

[115] Ekaterina Kozlyakova, Igor Danilovich, Anatoliy Volkov, Konstantin Zakharov, Olga Dimitrova, Elena Belokoneva, Larisa Shvanskaya, Elena Zvereva, Dmitry Chareev, Olga Volkova, et al. Tuning of physical properties of fe7 (po4) 6 by sodium intercalation. *Journal of Alloys and Compounds*, 744:600–605, 2018.

[116] EL Belokoneva, EA Ruchkina, and OV Dimitrova. Synthesis and crystal structure of new phosphate nafe42+ fe33+ [po4] 6. *Crystallography Reports*, 48(1):49–53, 2003.

[117] Alexey V Sobolev, Alena A Akulenko, Iana S Glazkova, Alexei A Belik, Takao Furubayashi, Larisa V Shvanskaya, Olga V Dimitrova, and Igor A Presniakov. Magnetic hyperfine interactions in the mixed-valence compound fe7 (po4) 6 from mössbauer experiments. *The Journal of Physical Chemistry C*, 122(34):19767–19776, 2018.

[118] Andreas Dönni, Lukas Keller, Vladimir Y Pomjakushin, Naohito Tsujii, and Alexei A Belik. Magnetic structures and magnetic phase diagram of the mixed-valence iron phosphate fe7 (po4) 6. *Inorganic Chemistry*, 65(13):7418–7430, 2026.

[119] OV Yakubovich, MA Simonov, Yu K Egorov-Tismenko, and NV Belov. The crystal structure of a synthetic variety of alluaudite na 2 (fe 3+ 0.5 fe 2+ 0.5) 2 fe 2+[po 4] 3. In *Soviet Physics Doklady*, volume 22, page 550, 1977.

[120] DR Corbin, JF Whitney, WC Fultz, GD Stucky, MM Eddy, and AK Cheetham. Synthesis of open-framework transition-metal phosphates using organometallic precursors in acidic media. preparation and structural characterization of fe5p4o20h10 and nafe3p3o12. *Inorganic Chemistry*, 25(14):2279–2280, 1986.

[121] Weifeng Huang, Biao Li, Muhammad Farooq Saleem, Xiang Wu, Jianjian Li, Jun Lin, Dingguo Xia, Wangsheng Chu, and Ziyu Wu. Self-assembled alluaudite na2fe3- xmnx (po4) 3 micro/nanocompounds for sodium-ion battery electrodes: A new insight into their electronic and geometric structure. *Chemistry–A European Journal*, 21(2):851–860, 2015.

[122] Dan Liu and G Tayhas R Palmore. Synthesis, crystal structure, and electrochemical properties of alluaudite na1. 702fe3 (po4) 3 as a sodium-ion battery cathode. *ACS Sustainable Chemistry & Engineering*, 5(7):5766–5771, 2017.

[123] Rachid Essehli, Hamdi Ben Yahia, Ruhul Amin, Fadwa El-Mellouhi, and Ilias Belharouak. Selective sodium-ion diffusion channels in na2-xfe3 (po4) 3 positive electrode for na-ion batteries. *Energy Storage Materials*, 24:343–350, 2020.

[124] Katarzyna Walczak, Andrzej Kulka, and Janina Molenda. Alluaudite-na1. 47fe3 (po4) 3: Structural and electrochemical properties of potential cathode material for na-ion batteries. *Solid State Sciences*, 87:21–26, 2019.

[125] TA Kurova, NG Shumyatskaya, Aleksandr Aleksandrovich Voronkov, and Yu A Pyatenko. Crystal structure of sidorenkite na 3 mn (po 4)(co 3). In *Soviet Physics Doklady*, volume 25, page 156, 1980.

[126] SV Krivovichev, AP Chernyatieva, SN Britvin, VN Yakovenchuk, and VG Krivovichev. Refinement of the crystal structure of bonshtedtite, na3fe (po4)(co3). *Geology of Ore Deposits*, 55(8):669–675, 2013.

[127] Hailong Chen, Qing Hao, Olivera Zivkovic, Geoffroy Hautier, Lin-Shu Du, Yuanzhi Tang, Yan-Yan Hu, Xiaohua Ma, Clare P Grey, and Gerbrand Ceder. Sidorenkite (na3mnpo4co3): a new intercalation cathode material for na-ion batteries. *Chemistry of Materials*, 25(14):2777–2786, 2013.

[128] Geoffroy Hautier, Anubhav Jain, Hailong Chen, Charles Moore, Shyue Ping Ong, and Gerbrand Ceder. Novel mixed polyanions lithium-ion battery cathode materials predicted by high-throughput ab initio computations. *Journal of Materials Chemistry*, 21(43):17147–17153, 2011.

[129] Xuemei Zeng, Kun He, Xiaomei Li, Yanshuai Li, and Yifei Yuan. The role of tunnel-structured hollandite material family for advancing energy storage applications. *Advanced Functional Materials*, page 2503135, 2025.

[130] M Latroche, L Brohan, R Marchand, and M Tournoux. New hollandite oxides: Tio2 (h) and k0. 06tio2. *Journal of Solid State Chemistry*, 81(1):78–82, 1989.

[131] Jae Hyeon Jo, Hee Jae Kim, Najma Yaqoob, Kyuwook Ihm, Oliver Guillon, Kee-Sun Sohn, Naesung Lee, Payam Kaghazchi, and Seung-Taek Myung. Hollandite-type potassium titanium oxide with exceptionally stable cycling performance as a new cathode material for potassium-ion batteries. *Energy storage materials*, 54:680–688, 2023.

[132] Yu Liu and Yefeng Yang. Recent progress of tio2-based anodes for li ion batteries. *Journal of Nanomaterials*, 2016(1):8123652, 2016.

[133] Anthony G Dylla, Graeme Henkelman, and Keith J Stevenson. Lithium insertion in nanostructured tio2 (b) architectures. *Accounts of chemical research*, 46(5):1104–1112, 2013.

[134] Mitsumasa Sakao, Norihito Kijima, Junji Akimoto, and Takeshi Okutani. Lithium insertion and extraction properties of hollandite-type kxtio2 with different k content in the tunnel space. *Solid State Ionics*, 243:22–29, 2013.

[135] Yonggang Wang, Ping He, and Haoshen Zhou. Olivine lifepo 4: development and future. *Energy & Environmental Science*, 4(3):805–817, 2011.

[136] Yujie Zhu, Yunhua Xu, Yihang Liu, Chao Luo, and Chunsheng Wang. Comparison of electrochemical performances of olivine nafepo 4 in sodium-ion batteries and olivine lifepo 4 in lithium-ion batteries. *Nanoscale*, 5(2):780–787, 2013.

[137] YZ Dong, YM Zhao, and H Duan. Crystal structure and lithium electrochemical extraction properties of olivine type lifepo4. *Materials Chemistry and Physics*, 129(3):756–760, 2011.

[138] Yongjin Fang, Qi Liu, Lifen Xiao, Xinping Ai, Hanxi Yang, and Yuliang Cao. High-performance olivine nafepo4 microsphere cathode synthesized by aqueous electrochemical displacement method for sodium ion batteries. *ACS applied materials & interfaces*, 7(32):17977–17984, 2015.

[139] Ghulam Ali, Ji-Hoon Lee, Dieky Susanto, Seong-Won Choi, Byung Won Cho, Kyung-Wan Nam, and Kyung Yoon Chung. Polythiophene-wrapped olivine nafepo4 as a cathode for na-ion batteries. *ACS applied materials & interfaces*, 8(24):15422–15429, 2016.

[140] Peng Shan, Yue Gu, Luyi Yang, Tongchao Liu, Jiaxin Zheng, and Feng Pan. Olivine fepo4 cathode material for rechargeable mg-ion batteries. *Inorganic Chemistry*, 56(21):13411–13416, 2017.

[141] Bertan Özdogru, Behrad Koohbor, and Ö Özgür Çapraz. The impact of alkali-ion intercalation on redox chemistry and mechanical deformations: Case study on intercalation of li, na, and k ions into fepo4 cathode. *Electrochemical Science Advances*, 2(4):e2100106, 2022.

[142] Sanghyeon Kim, Liang Yin, Myeong Hwan Lee, Prakash Parajuli, Lauren Blanc, Timothy T Fister, Haesun Park, Bob Jin Kwon, Brian J Ingram, Peter Zapol, et al. High-voltage phosphate cathodes for rechargeable ca-ion batteries. *ACS Energy Letters*, 5(10):3203–3211, 2020.

[143] Shyue Ping Ong, Vincent L Chevrier, Geoffroy Hautier, Anubhav Jain, Charles Moore, Sangtae Kim, Xiaohua Ma, and Gerbrand Ceder. Voltage, stability and diffusion barrier differences between sodium-ion and lithium-ion intercalation materials. *Energy & Environmental Science*, 4(9):3680–3688, 2011.

[144] Jongsoon Kim, Dong-Hwa Seo, Hyungsub Kim, Inchul Park, Jung-Keun Yoo, Sung-Kyun Jung, Young-Uk Park, William A Goddard III, and Kisuk Kang. Unexpected discovery of low-cost maricite nafepo4 as a high-performance electrode for na-ion batteries. *Energy & Environmental Science*, 8(2):540–545, 2015.

[145] O Garcia-Moreno, M Alvarez-Vega, F Garcia-Alvarado, J Garcia-Jaca, JM Gallardo-Amores, ML Sanjuán, and U Amador. Influence of the structure on the electrochemical performance of lithium transition metal phosphates as cathodic materials in rechargeable lithium batteries: a new high-pressure form of limpo4 (m= fe and ni). *Chemistry of materials*, 13(5):1570–1576, 2001.

[146] Elena Aleksandrovna Genkina, Boris Alekseevich Maksimov, Yurii Konstantinovich Kabalov, and Oleg Konstantinovich Melnikov. Crystal structure of li,fe-metaphosphate lifep_3o_9. In *Doklady Akademii Nauk*, volume 270, pages 1113–1116. Russian Academy of Sciences, 1983.

[147] Hailong Chen, Geoffroy Hautier, and Gerbrand Ceder. Synthesis, computed stability, and crystal structure of a new family of inorganic compounds: carbonophosphates. *Journal of the American Chemical Society*, 134(48):19619–19627, 2012.

[148] Zhaoheng Liang, Fei Tian, Gongzheng Yang, and Chengxin Wang. Enabling long-cycling aqueous sodium-ion batteries via mn dissolution inhibition using sodium ferrocyanide electrolyte additive. *Nature Communications*, 14(1):3591, 2023.